Bulky phosphine ligands promote palladium-catalyzed protodeboronation

Cher Tian Ser[1,2†], Han Hao[1,3†], Sergio Pablo-García[1,2,3], Kjell Jorner[1‡], Shangyu Li[1], Robert Pollice[1§]* and Alán Aspuru-Guzik[1,2,3,4,5,6,7]*

[1] Chemical Physics Theory Group, Department of Chemistry, University of Toronto, 80 St. George St, Toronto, Ontario M5S 3H6, Canada

[2] Vector Institute for Artificial Intelligence, W1140-108 College St, Toronto, Ontario M5G 0C6, Canada

[3] Acceleration Consortium, 700 University Ave, Toronto, Ontario M5G 1Z5, Canada

[4] Department of Computer Science, University of Toronto, 40 St. George St, Toronto, Ontario M5S 2E4, Canada

[5] Department of Chemical Engineering & Applied Chemistry, 200 College St, University of Toronto, Ontario M5S 3E5, Canada

[6] Department of Materials Science & Engineering, 184 College St, University of Toronto, Ontario M5S 3E4, Canada

[7] Lebovic Fellow, Canadian Institute for Advanced Research (CIFAR), 661 University Ave, Toronto, Ontario M5G, Canada.

[†] These authors contributed equally to this work.

[‡] Current address: Institute of Chemical and Bioengineering, Department of Chemistry and Applied Biosciences, ETH Zurich, Vladimir-Prelog-Weg 1, CH-8093 Zürich, Switzerland

[§] Current address: Stratingh Institute for Chemistry, University of Groningen, Nijenborgh 4, Groningen, 9747 AG, The Netherlands

*Corresponding authors: r.pollice@rug.nl, aspuru@utoronto.ca

Abstract

The Suzuki-Miyaura cross-coupling reaction is plagued by protodeboronation, an undesirable side reaction with water that consumes the boronic acid derivatives required for the cross-coupling reaction. Meticulous mechanistic studies have previously established protodeboronation to be highly sensitive to the nature of the boronic reagent and reaction conditions. Particularly, the presence of bases, which are essential for the Suzuki-Miyaura coupling, is known to catalyze protodeboronation. However, protodeboronation catalyzed by palladium-phosphine complexes, the benchmark catalyst system for Suzuki-Miyaura cross-coupling, has been largely overlooked. We demonstrate, using automated high-throughput experimentation, comprehensive computational mechanistic analyses and kinetic modeling, that protodeboronation is accelerated by palladium(II) complexes bound to bulky phosphine ligands. While sterically hindered ligands are typically used to facilitate difficult cross-couplings, these ligands can instead paradoxically impede cross-coupling product formation, requiring careful and judicious consideration when choosing ligands for Suzuki-Miyaura cross-couplings.

Introduction

One of the most important uses of organoboron reagents is as a nucleophilic coupling partner in the Nobel-prize winning Suzuki-Miyaura cross-coupling (SMC) reaction, the most popular reaction for C-C bond formations, due to its low toxicity, ease of handling, and robustness.[1–4] However, organoboron compounds can be unstable in moisture, and undergo protodeboronation (PDB), yielding protoarenes *via* the loss of the boronic moiety. This side reaction has been identified by Kuivila et al. as one of the major degradation pathways of organoboron compounds even before their extensive applications in cross-coupling reactions.[5–8] While PDB can either be a useful chemical transformation or leveraged as a means to decompose unreacted substrates during work-up,[9–14] it is largely considered an undesirable and unproductive side reaction.

As the SMC occurs under basic conditions and is often conducted under at least partially aqueous conditions, the base-catalyzed PDB of arylboronic acid derivatives in aqueous media has received considerable attention.[7,15–17] In light of this, a wide variety of strategies has been implemented to minimize PDB. One prominent strategy is through ligand design, as it is well-known that the ligand controls the activity of the palladium catalyst.[18,19] Efforts to facilitate the SMC have been achieved with dialkylbiaryl phosphine ligands, introduced by Buchwald and co-workers, which promotes catalytic turnover by stabilizing reactive monoligated palladium species.[18,19] Thus, efficient cross-coupling product formation can be achieved *via* ligand design towards faster product formation to outcompete protodeboronative pathways.[18] At the same time, protective groups or reagents like trialkoxy-ligated boronate salts, trifluoroborates, or MIDA boronates that slowly supply their corresponding boronic acids over the course of the reaction further reduces the degree of PDB.[20] However, these strategies may not always be effective, particularly for sterically hindered or electron-deficient arylboronic acid derivatives.[16,21]

Amongst other metals,[6,9,22–25] PDB has also been shown to be catalyzed by palladium complexes,[10–12,23] the most common catalytic system for the SMC. Surprisingly, despite the popularity of the SMC, there is a lack of detailed investigation into palladium-catalyzed PDB, and the role of the ligand in controlling PDB under conditions relevant to the SMC.[20,26] Instead, the SMC is typically performed with an excess of boronic reagents to compensate for the loss *via* PDB, resulting in extensive downstream purifications, and the wasteful expenditure of expensive boronic reagents. Contrary to predominant notions in the literature where PDB is primarily considered to be base-catalyzed in the context of the SMC,[7,15–17] in this work, we demonstrate, both experimentally and computationally, that sterically hindered phosphine ligands promote palladium-catalyzed PDB of boronic acid derivatives. Our *ab initio* mechanistic investigations reveal that sterically hindered phosphines favor the formation of an unstable post-transmetalation species that leads to facile PDB, while sterically compact phosphines favor the formation of a stable palladium-boron intermediate that prevents PDB. Through detailed kinetic modeling of the competitive rates of each protodeboronative pathway derived from reaction barriers obtained from density functional theory (DFT),

we achieve semi-quantitative yield predictions for our ligands. Finally, our statistical analysis reveals a simple steric descriptor for phosphine ligands that correlates well with the degree of palladium-catalyzed PDB, guiding ligand selection for improved SMC yields.
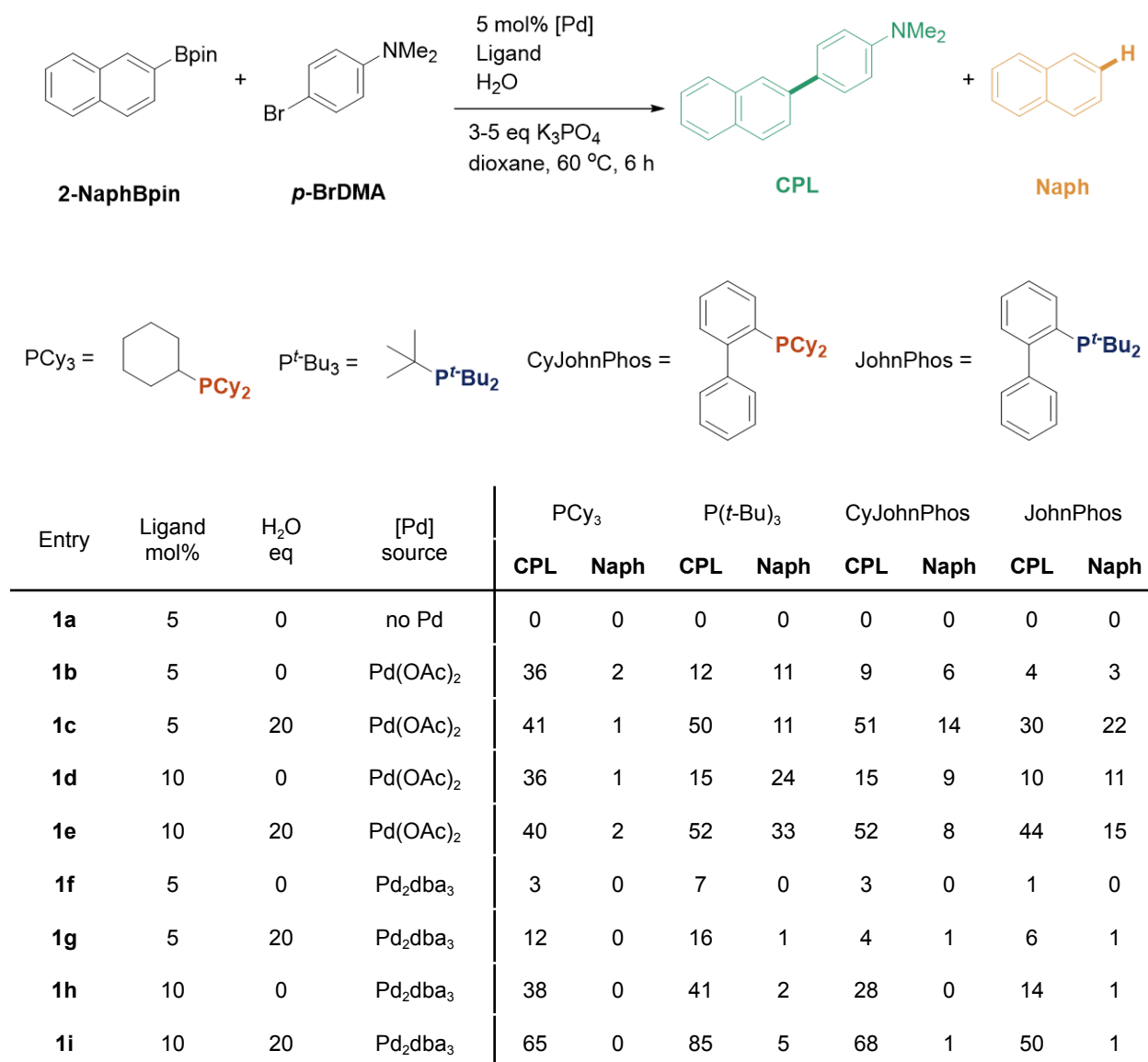
Results and Discussion

Competitive catalytic protodeboronation versus Suzuki-Miyaura cross-coupling
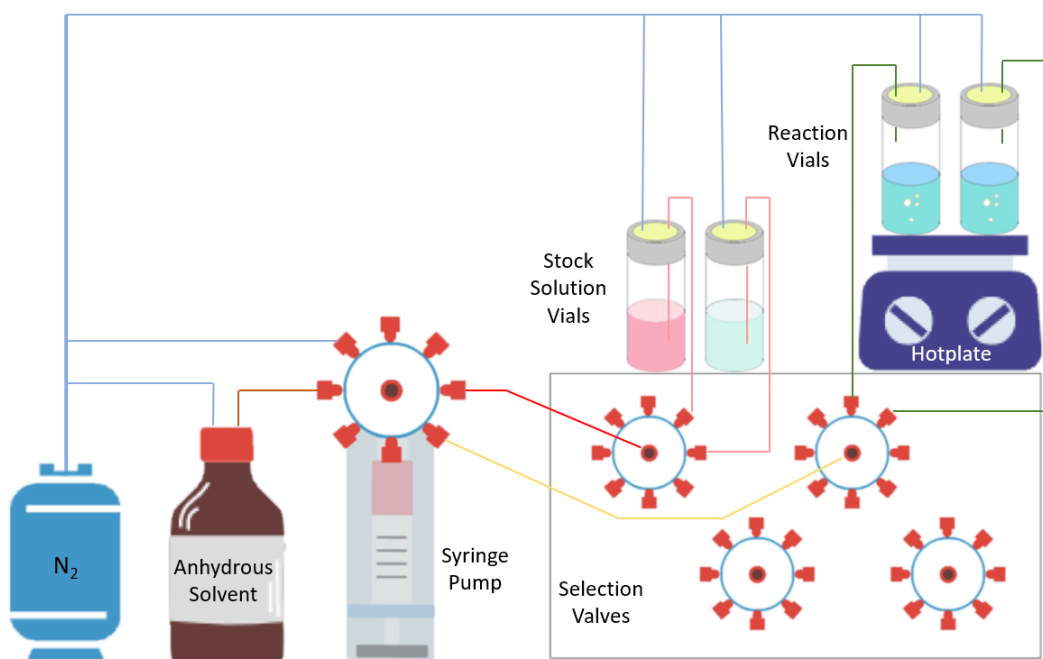
Figure 1: Hardware configuration of the high-throughput reaction screening variant of MEDUSA.

3

Table 1: Cross-coupled (**CPL**) and protodeboronated (**Naph**) product yields in % of the palladium-catalyzed SMC of 2-naphthalene boronic acid pinacol ester (**2-NaphBpin**) and *para*-bromodimethylaniline (**p-BrDMA**) with varied ligands and water amounts (**x**). Yields are estimated with HPLC based on duplicate experiments. Inaccuracies in K_3PO_4 equivalents were introduced in rapid manual dosing (see **Experimental Procedures**). See **Supplementary Discussion S2.2** for the full range of conditions assessed.

Entry	Ligand mol%	H_2O eq	[Pd] source	PCy$_3$		P(t-Bu)$_3$		CyJohnPhos		JohnPhos	
				CPL	**Naph**	**CPL**	**Naph**	**CPL**	**Naph**	**CPL**	**Naph**
1a	5	0	no Pd	0	0	0	0	0	0	0	0
1b	5	0	Pd(OAc)$_2$	36	2	12	11	9	6	4	3
1c	5	20	Pd(OAc)$_2$	41	1	50	11	51	14	30	22
1d	10	0	Pd(OAc)$_2$	36	1	15	24	15	9	10	11
1e	10	20	Pd(OAc)$_2$	40	2	52	33	52	8	44	15
1f	5	0	Pd$_2$dba$_3$	3	0	7	0	3	0	1	0
1g	5	20	Pd$_2$dba$_3$	12	0	16	1	4	1	6	1
1h	10	0	Pd$_2$dba$_3$	38	0	41	2	28	0	14	1
1i	10	20	Pd$_2$dba$_3$	65	0	85	5	68	1	50	1

In the course of our experimental investigations in a prior work, a significant amount of PDB product was observed when preparing extended conjugated systems for organic lasers using the SMC, despite relatively mild conditions being applied (**Supplementary Table S2**).[27] Noteworthily, base-mediated PDB was not observed, and instead significant amounts of protodeboronated reactants formed with the

4

introduction of palladium. Thus, to explore this phenomenon further, we evaluated the competitive formation of cross-coupled (**CPL**) and protodeboronated (**Naph**) products using a model reaction, performed under typical SMC reaction conditions with different palladium sources, ligand identities and loadings, water amounts and temperatures (**Table 1, Supplementary Discussion S2.3**). As unprotected electron-deficient and heteroaromatic boronic acid derivatives tend to undergo base-catalyzed PDB very rapidly,[15,16] preventing cross-coupling or the ability to distinguish between palladium-catalyzed or base-catalyzed PDB, we chose the electron-neutral 2-naphthalene boronic acid pinacol ester (**2-NaphBpin**) with a protected boronic ester group. Furthermore, since the SMC is generally rapid and dominant with good coupling partners like aryl iodides which makes it challenging to investigate the reaction details, we selected *para*-bromodimethylaniline (***p*-BrDMA**) to modulate the reactivity for our model reaction. Due to the large volume of experiments (>100, each performed in duplicate) and the requirement of precise reagent handling (<±2.5% of 1 mg) under an inert atmosphere, manual operation becomes infeasible considering the labor and possible errors associated. As automated high-throughput experiments (HTE) with robotic systems have shown their superior performance over traditional screening approaches, especially in the scenario of cross-coupling reaction optimization campaigns,[28] we fully leverage the potential of robotic synthesis and screening by implementing an automated strategy using an automated dosing robot and the HTE variant of our modular robotic synthesis platform MEDUSA (**Figure 1**).[29,30]

Unsurprisingly, there was negligible formation of **CPL** without the presence of palladium (**Table 1, Entry 1a**). Interestingly, the presence of **Naph** was negligible as well, showing the pinacol esters' resistance to base-catalyzed PDB under our conditions in the absence of metals.[16,17] When palladium is present, we observed promoted formation of the PDB byproduct **Naph** alongside the expected SMC product **CPL**. In addition to the known ligand effect in the palladium-catalyzed SMC, to our surprise, we also observed a significant effect of phosphine structure on **Naph** yields. Generally, cyclohexyl-substituted (Cy) phosphines show higher reactivity than their *tert*-butyl (*t*-Bu) counterparts in catalyzing productive **CPL** formation over undesirable **Naph** formation. With $Pd(OAc)_2$ as the palladium source, PCy_3 leads to <1% **Naph** yields and modest to high **CPL** yields in almost all cases (**Table 1, Entries 1b-1e**), while *t*-Bu-substituted phosphines lead to the significant formation of **Naph,** which in several cases have yields comparable to **CPL**. Notably, **Naph** yields can be significant when *t*-Bu substituted phosphines are used under relatively dry conditions commonly used in organic synthesis (see **Experimental Methods**), suggesting that adventitious water is enough to cause PDB.

The yields of **Naph** generally increase across different ligands when 20 eq. of H_2O is added to the reaction. We attribute this to the increased concentration of H_2O, which can provide the hydrogen atom replacing the boronic moiety through PDB (**Entry 1c, 1e** vs **1b, 1d**). At the same time, the addition of H_2O promotes **CPL** yields compared to anhydrous conditions, which was previously observed in reported

5

mechanistic studies of the SMC.[31–34] Notably, the ratio of **CPL**:**Naph** products generally increases significantly with the addition of 20 eq. of H_2O. This suggests that even though PDB is facilitated with higher H_2O content, performing the SMC under partially aqueous conditions is still beneficial to improve the selectivity for cross-coupled products.[35] Increasing the palladium loading from 5 mol% to 10 mol% does not lead to proportional increases of either **CPL** or **Naph** yields, suggesting the existence of complicated off-cycle equilibria and/or catalyst deactivation processes (**Entry 1d, 1e vs 1b, 1c**).
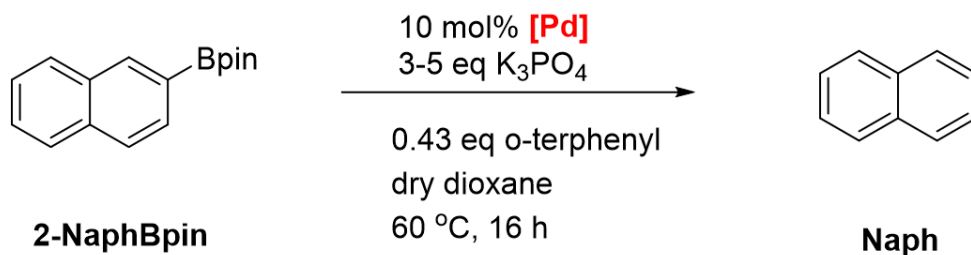
Since most palladium-catalyzed reactions, including the SMC, involve Pd(0)-Pd(II) cycles, we further evaluated Pd_2dba_3 as the Pd(0) source (**Entries 1f-1i**). The yields of **Naph** are generally negligible and yields of **CPL** are generally much higher, revealing more efficient SMC over PDB. Therefore, Pd(0) species likely play a minor role in palladium-catalyzed PDB, unlike their dominant role in the SMC catalytic cycle. Similar to previous observations, adding 20 eq. H_2O promotes the yield of **CPL** (**Entry 1g, 1i vs 1f, 1h**), but **CPL** yields are affected more significantly when ligand equivalents are increased to 2 eq., as excess phosphines are required to replace the dba ligand and generate mononuclear Pd(0) active species (**Entry 1h, 1i vs 1f, 1g**).

Screening conditions for palladium-catalyzed protodeboronation

Having established that PDB can be promoted by phosphine-ligated palladium complexes, we focused on understanding the key factors of PDB without the presence of a coupling partner. Such a simplified system avoids the complicated equilibria in the SMC reaction mixture, and allows us to dive deeper into how the palladium source, ligand identity and loading, base identity, and water content directly affect palladium-catalyzed PDB.

We first performed experiments to investigate the impact of the palladium source on PDB under conditions typically used in the SMC with K_3PO_4 as the base (**Table 2, Supplementary Discussion S3.1**). Similar to the observations in the competitive reactions, no PDB happens without palladium (**Entry 2a**). This is consistent with the fact that electron-neutral boronic reagents are not prone to base-catalyzed PDB (**Supplementary Discussion S6.1**) and our earlier results in the competitive cross-coupling experiments (**Table 1**). Interestingly, PDB does not happen with palladium alone without ligands, regardless of the palladium source (**Entries 2b, 2h, 2m**). As a significant amount of Pd black forms in these reactions (**Supplementary Figure S13**), we suspect that the lack of stabilizing ligands leads to catalyst poisoning under basic conditions, and therefore a lack of palladium-catalyzed PDB. This evidence is consistent with Kuivila et al.'s seminal work on metal-catalyzed PDB, where they were not able to obtain kinetic data for $PdCl_2$ in an aqueous buffer solution.[36] This is also consistent with our proposed mechanism for palladium-catalyzed PDB by unligated palladium (**Supplementary Discussion S6.2**).

Table 2 Yields and errors of palladium-catalyzed protodeboronation (**Naph**) with different palladium sources using K_3PO_4 as base at 60 °C. *: in the form of HBF_4 salt. **: errors were not included for yields <0.1%.
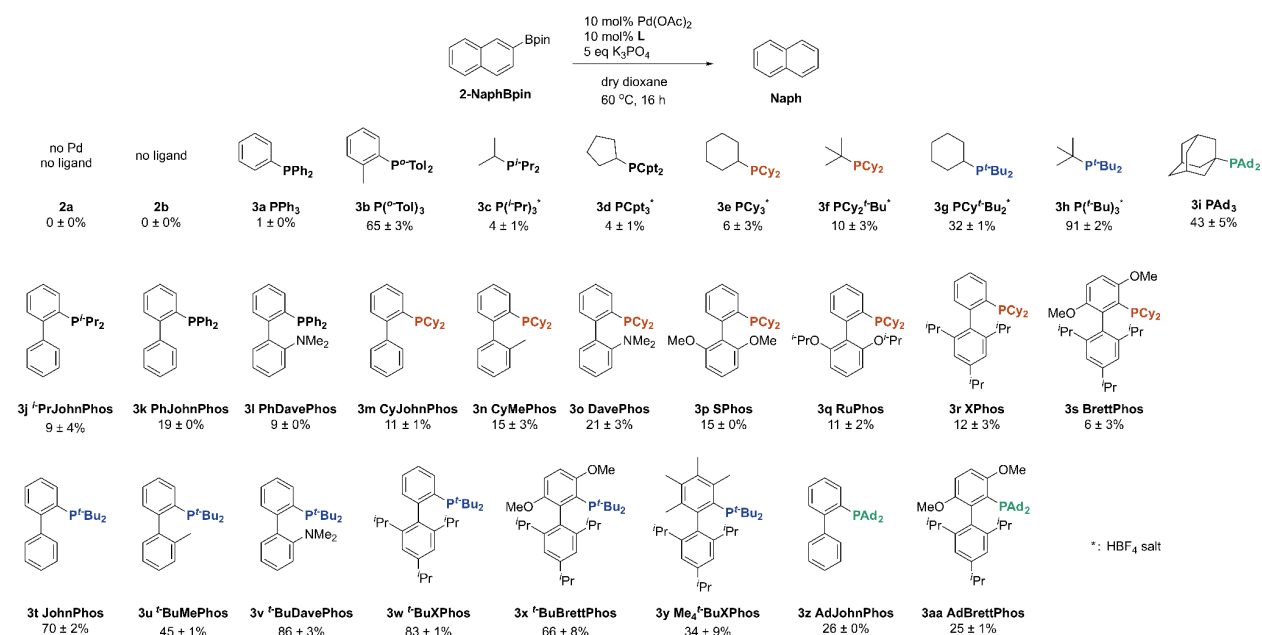
10 mol% **[Pd]**
3-5 eq K_3PO_4

2-NaphBpin → **Naph**

0.43 eq o-terphenyl
dry dioxane
60 °C, 16 h

Entry	Palladium source	**Naph** / %
2a	No Pd	0**
2b	$Pd(OAc)_2$	0**
2c	$Pd(OAc)_2$ + P(t-Bu)$_3$*	91 ± 2
2d	$Pd(OAc)_2$ + JohnPhos	70 ± 3
2e	$Pd(OAc)_2$ + PCy$_3$*	6 ± 3
2f	$Pd(OAc)_2$ + CyJohnPhos	11 ± 1
2g	$Pd(OAc)_2$ + XPhos	12 ± 3
2h	$PdCl_2$	0**
2i	$PdCl_2$ + P(t-Bu)$_3$*	68 ± 4
2j	$PdCl_2$ + JohnPhos	22 ± 1
2k	$PdCl_2$ + PCy$_3$*	0**
2l	$PdCl_2$ + CyJohnPhos	1 ± 0
2m	Pd_2dba_3	0**
2n	Pd_2dba_3 + P(t-Bu)$_3$*	26 ± 3
2o	Pd_2dba_3 +JohnPhos	4 ± 1
2p	Pd_2dba_3 + PCy$_3$*	3 ± 0
2q	Pd_2dba_3 + CyJohnPhos	3 ± 0
2r	P(t-Bu)$_3$ Pd G4	72 ± 6
2s	JohnPhos Pd G4	6 ± 0
2t	XPhos Pd G2	16 ± 3

With $Pd(OAc)_2$ as the palladium source, the *t*-Bu-substituted ligands P(*t*-Bu)$_3$ and JohnPhos lead to >70% **Naph** yields, while the Cy-substituted ligands PCy$_3$, CyJohnPhos and XPhos lead to <15% **Naph** yields (**Entries 2c-2g**). As these results align well with the observations in the competitive reactions (**Table 1**), we believe that the reactivities obtained here without the coupling partner are representative of the

7

palladium-catalyzed PDB in the presence of the aryl halide coupling reagent. Using PdCl$_2$ as a Pd(II) source reproduces the ligand-dependent trend with slightly less **Naph** yields (**Entries 2h-2l**), while significantly reduced **Naph** yields are observed when switching to Pd$_2$dba$_3$ as a Pd(0) source (**Entries 2m-2q**). We note that AcO$^-$ is known to promote the reduction of Pd(II) to Pd(0),[37,38] and halides other than F$^-$ cannot,[39] suggesting that the role of the counterion is minimal in palladium-catalyzed PDB. Using preformed palladacycles which generate Pd(0) rapidly in contact with base leads to highly ligand dependent reactivity (**Entries 2r-2t**). These results further strengthen the major role of Pd(II) species in palladium-catalyzed PDB over Pd(0) species, which reiterates findings in the competitive cross-coupling reactions (**Table 1**).

Table 3: Yields of protodeboronated product (**Naph**) from the palladium-catalyzed protodeboronation of 2-naphthalene boronic acid pinacol ester (**2-NaphBpin**) with various phosphine ligands. Inaccuracies in K$_3$PO$_4$ equivalents were introduced in rapid manual dosing (see **Experimental Procedures**). Yields and errors are estimated with HPLC based on duplicate experiments.

Reaction scheme: **2-NaphBpin** → (10 mol% Pd(OAc)$_2$, 10 mol% **L**, 5 eq K$_3$PO$_4$, dry dioxane, 60 °C, 16 h) → **Naph**

Entry	Ligand	Yield
2a	no Pd, no ligand	0 ± 0%
2b	no ligand	0 ± 0%
3a	PPh$_3$	1 ± 0%
3b	P(o-Tol)$_3$	65 ± 3%
3c	P(i-Pr)$_3$*	4 ± 1%
3d	PCpt$_3$*	4 ± 1%
3e	PCy$_3$*	6 ± 3%
3f	PCy$_2$^{t}Bu*	10 ± 3%
3g	PCy^{t}Bu$_2$*	32 ± 1%
3h	P(tBu)$_3$*	91 ± 2%
3i	PAd$_3$	43 ± 5%
3j	^{i}PrJohnPhos	9 ± 4%
3k	PhJohnPhos	19 ± 0%
3l	PhDavePhos	9 ± 0%
3m	CyJohnPhos	11 ± 1%
3n	CyMePhos	15 ± 3%
3o	DavePhos	21 ± 3%
3p	SPhos	15 ± 0%
3q	RuPhos	11 ± 2%
3r	XPhos	12 ± 3%
3s	BrettPhos	6 ± 3%
3t	JohnPhos	70 ± 2%
3u	^{t}BuMePhos	45 ± 1%
3v	^{t}BuDavePhos	86 ± 3%
3w	^{t}BuXPhos	83 ± 1%
3x	^{t}BuBrettPhos	66 ± 8%
3y	Me$_4$^{t}BuXPhos	34 ± 9%
3z	AdJohnPhos	26 ± 0%
3aa	AdBrettPhos	25 ± 1%

*: HBF$_4$ salt

Having established that bulky phosphines tend to promote PDB with Pd(II) sources, we expanded the screening scope to 27 phosphines to comprehensively study the ligand dependency of palladium-catalyzed PDB, using Pd(OAc)$_2$ as the palladium source (**Table 3, Supplementary Discussion S3.2**). Similar to results in the competitive cross-coupling experiments (**Table 1**), both palladium and phosphine ligands are required for PDB (**Table 2, Table 3, 2a-b**), and a wide range of **Naph** yields are observed across different phosphines, with bulky phosphines having higher **Naph** yields than their less sterically-congested counterparts. This is most apparent when comparing PPh$_3$ (**Table 3, 3a**) and P(o-tol)$_3$ (**Table 3, 3b**), and in the increased **Naph** yields of the P(t-Bu)$_x$(Cy)$_{3-x}$ series with increasing x (**Table 3,**

3e-3h). We observe similar trends with Buchwald ligands, where bulky *t*-Bu (**Table 3, 3t-3y**) groups lead to increased **Naph** yields compared to their less bulky isopropyl and phenyl (**Table 3, 3j-3l**) or cyclohexyl (**Table 3, 3m-3s**) counterparts. However, elevating the steric congestion around the phosphorus atom by replacing phenyl with biphenyl (**Table 3, 3a** vs **3j**) or by increasing biphenyl bulkiness of the dicyclohexyl Buchwald ligands (**Table 3, 3m** vs **3n-s**) does not significantly promote PDB, suggesting that steric bulk further away from the phosphorus atom is less effective at promoting PDB. While the extra-bulky 1-adamantyl phosphines (**Table 3, 3i, 3z, 3aa**) show increased PDB compared to their cyclohexyl variants (**Table 3, 3e, 3m, 3s**), they show inferior PDB compared to their *t*-Bu analogs (**Table 3, 3h, 3t, 3x**). Small amounts of binaphthalene from homocoupling were observed as a minor by-product (**Supplementary Table S5, Supplementary Figure S14**). However, the yields of binaphthalene were generally below 5%, precluding the elucidation of any significant trends. We propose that binaphthalene forms through oxidative coupling with either Pd(II) as an oxidant or trace amounts of residual oxygen, despite the extensive degassing in our workflow.[40,41]

Increasing the palladium and phosphine loadings simultaneously does not lead to an observable increase of **Naph** yields, and instead inconsistent trends were observed (**Supplementary Discussion S3.3**). While for most phosphines the **Naph** yields either increased slightly or did not change, for JohnPhos the **Naph** yields decreased with higher palladium-phosphine loadings (**Supplementary Table S6, Supplementary Figure S15**). Considering the prolonged reaction time of 16 h, we propose the overall end-point **Naph** yields are determined by catalyst deactivation and/or reaction equilibrium, which we confirmed by reaction kinetic monitoring (*vide infra*). Interestingly, since phosphines are known to reduce Pd(II) to Pd(0) in the presence of base,[37,42] we expected that an increase in phosphine equivalents would inhibit PDB by promoting palladium reduction. However, while phosphines are essential for palladium-catalyzed PDB, increasing L:Pd ratios does not result in decreased **Naph** yields as expected, and using up to four equivalents of phosphine slightly promoted PDB instead (**Supplementary Discussion S3.4**).

We additionally investigated the base dependency of palladium-catalyzed PDB across 16 inorganic and organic bases, using Pd(OAc)$_2$ as the palladium source and JohnPhos as the ligand (**Supplementary Discussion S3.5**). In summary, oxo-bases are essential for PDB, which is consistent with the oxophilicity of the boron moiety as a major driving force for the cleavage of B-R bonds, while weakly/non-coordinating bases (e.g. pyridine, DBU) are unable to drive the B-R cleavage, resulting in low PDB. Generally, stronger and more soluble bases promote PDB (**Supplementary Table S8**).[37,42,43] Despite the base choice having an effect on **Naph** yields, we note that the choice of ligand is still the dominating factor, as base screening experiments conducted with CyJohnPhos or unligated Pd(OAc)$_2$ show little variance in **Naph** yields, and in some cases even show zero PDB (**Supplementary Table S8, Entries 7b-l, 8b-l**). These results emphasize the fact that, under SMC conditions, the role of palladium-catalyzed PDB can be more significant than the base-catalyzed version of PDB.[15–17] However, NaH, KO(*t*-Bu), and NaO(*t*-Bu) cause significant PDB regardless of the choice of ligand or even under ligand-free conditions, suggesting that

9

caution should be exercised when using these bases with boronic reagents (**Supplementary Table S8, Entries 6-8e, 6-8g, 6-8k**).

As all the aforementioned PDB screening reactions were performed under "dry" conditions typically used in organic synthesis (bases were stored in desiccators or pre-dried in an oven, and dry N_2 atmosphere was applied (see **Experimental Methods**)), the source of H atom in the **Naph** product that replaces the boron moiety of **2-NaphBpin** was not clear. By intentionally introducing 20 eq. H_2O or D_2O, PDB reactions catalyzed by $Pd(OAc)_2$ and JohnPhos reach full conversion regardless of whether the reactions were performed in vials or in NMR tubes. Importantly, we recovered both 2-^{1}H-naphthalene and 2-^{2}D-naphthalene in a 1:4 ratio based on ^{1}H-NMR integration, suggesting that up to five equivalents of H_2O (0.025 mmol, ~0.06% V/V) exists in our reaction conditions (**Supplementary Figure S29, S36**). This suggests that the origin of the H atom is a protic hydrogen in H_2O, which aligns well with the established mechanism of base-catalyzed PDB (**Supplementary Discussion S6.1**).[16,17] We propose the water comes from adsorbed H_2O on bases and glasswares, which is known to be challenging to remove with "organic dry" protocols.[44,45]

Online monitoring and reaction kinetics

During the end-point analysis of reaction screening, we found that competing catalyst deactivation or off-cycle equilibria may happen along with the palladium-catalyzed PDB major pathway as established by the formation of Pd black after reaction (**Supplementary Figure S13**). Therefore, we performed kinetic experiments with the $Pd(OAc)_2$-JohnPhos-K_3PO_4 system to gain more insight into the reaction mechanism of palladium-catalyzed PDB. The modularity of the MEDUSA platform allowed us to set up automatic online monitoring *via* HPLC under an inert atmosphere, a capability which is not routinely available to common automated synthetic platforms (see **Figure 2a**, **Experimental Methods** and **Supplementary Discussion S4**). With **2-NaphBpin**, we identified a short induction period which we attribute to the heating up of the reaction mixture (**Supplementary Table S9-S18, Supplementary Figure S19-S25**). Afterwards, the formation of **Naph** increased roughly linearly. Based on the dependence of the corresponding initial rates on temperature, *via* the Arrhenius equation, we derived an enthalpic activation barrier of 18.1 kcal/mol for JohnPhos (**Figure 2b, 2c**), which is much lower than base (OH$^-$) catalyzed PDB for equivalent systems (**Supplementary Discussion S5.1**).[16] Additionally, half-lives of less than three hours were identified with P(*t*-Bu)$_3$ and JohnPhos as ligands, indicating faster reaction rates at lower temperature compared to the base-catalyzed variant, emphasizing the catalytic activity of palladium-phosphine complexes compared to base (**Figure 2d**, **Supplementary Figure S19-S20**). Finally, while the reaction yield increased linearly over 3 h for JohnPhos, the yield for CyJohnPhos significantly slowed down within 1 h, suggesting that the $Pd(OAc)_2$/CyJohnPhos system is sluggish in catalyzing PDB, possibly due to catalyst deactivation (**Supplementary Figure S20c**).

10
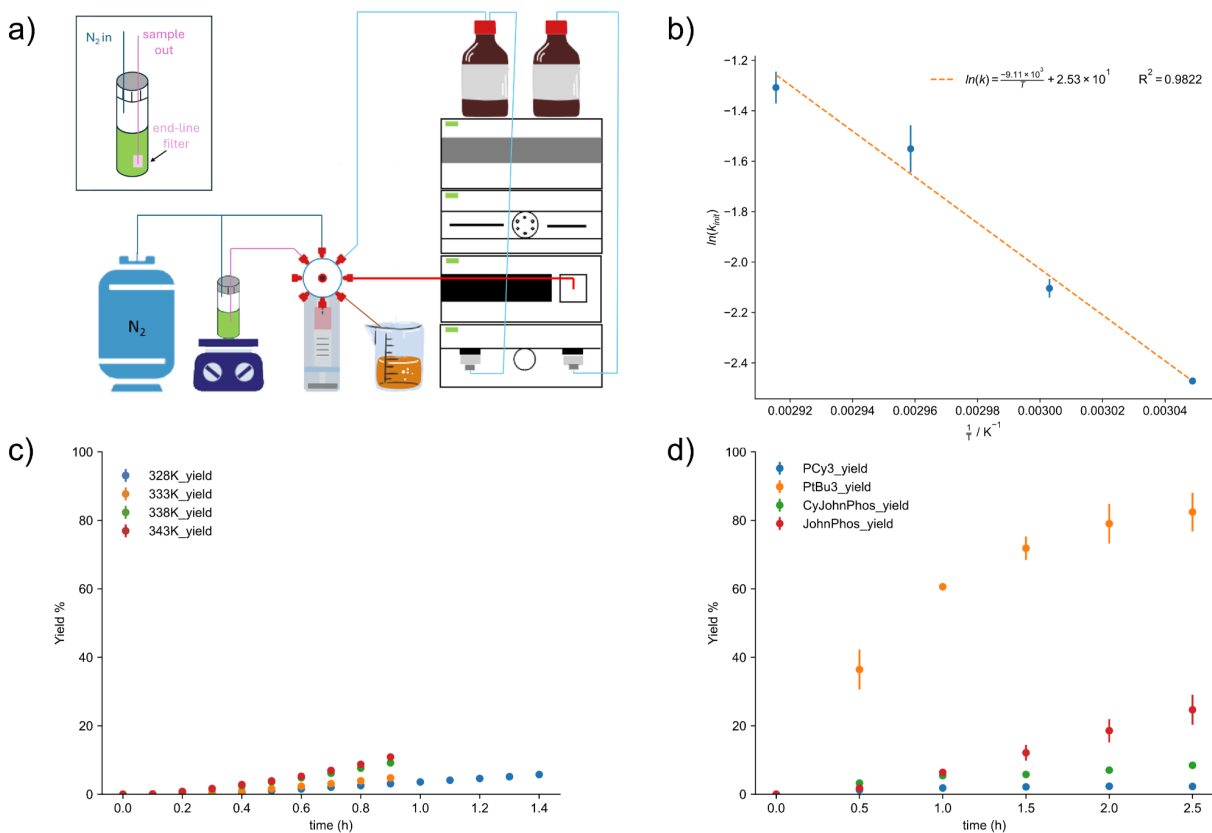
Figure 2: **a**) Hardware configuration of the continuous reaction monitoring variant of MEDUSA. **b**) ln(initial rate) vs 1/T (Arrhenius plot) of **Naph** *via* palladium-catalyzed PDB of **2-NaphBpin** using Pd(OAc)$_2$, JohnPhos and K$_3$PO$_4$ in dry dioxane. **c**) Monitoring of **Naph** formation *via* palladium-catalyzed PDB of **2-NaphBpin** over time using Pd(OAc)$_2$, JohnPhos and K$_3$PO$_4$ in dry dioxane. **d**) Ligand dependent palladium-catalyzed PDB reactivity as demonstrated by **Naph** formation *via* palladium-catalyzed PDB of **2-NaphBpin** over time using Pd(OAc)$_2$ and K$_3$PO$_4$ in dry dioxane.

Computational mechanistic investigations

To further elucidate the underlying reasons for the difference in palladium-catalyzed PDB between ligands, we computationally investigated the mechanism of palladium-catalyzed PDB using DFT (**Figure 3,** see **Computational Methods**). While both boronic esters and boronic acids are capable of directly transmetalating onto palladium without hydrolysis,[43,46] we chose to model the boronic reagent as a boronic acid, as boronic esters have been demonstrated to undergo facile hydrolysis under basic aqueous conditions, and that we had also experimentally identified trace amounts of 2-naphthalene boronic acid under our reaction conditions.[17]

11
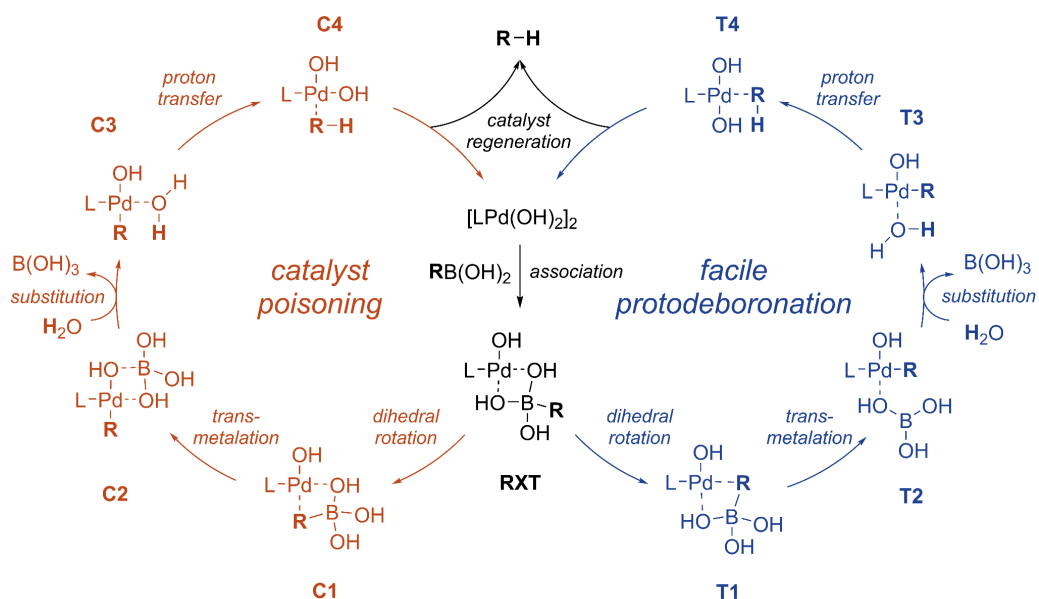
Figure 3: Proposed mechanism for palladium-catalyzed protodeboronation.

In our proposed mechanism for palladium-catalyzed PDB, the Pd(II) catalyst first associates with the boronic acid to form a mononuclear square-planar palladium-boron complex (**RXT**).[43,46] Thus, we need to identify the reference state of this Pd(II) catalyst. It is well known that Pd(II) forms a complex equilibrium of structures under PDB and SMC conditions,[47] but the structures of the major components of phosphine-supported palladium species in basic conditions have not yet been confirmed. Hence, we performed a systematic computational analysis to find an appropriate reference state by considering the coordination of palladium to various Lewis bases within our experimental conditions. We found that, in general, the mononuclear palladium-phosphine species $LPd(OH)_2$, when either uncoordinated or coordinated to various Lewis bases (H_2O, dioxane, phosphine), showed large differences in computed energies compared to the proposed mononuclear square-planar palladium-boron complex **RXT**. Additionally, there was a large variation in stability of the investigated reference states between phosphine ligands. Our analysis reveals that representing the reference state as the dinuclear Pd(II) catalyst $[LPd(OH)_2]_2$ offered consistency in relative stability to **RXT** and between ligands, which is why we chose this as the reference state for the analysis below (see **Supplementary Discussion S7.2** for a detailed analysis on other mononuclear or oligomeric reference states). We also note that while the choice of the reference state is necessary to define a state the catalyst returns to after one turnover cycle for our computational microkinetic analysis, it has no impact on the selectivity between the different pathways, which is represented by the yield of **Naph** at the end of the kinetic campaign.

After the association of the boronic acid to the dinuclear Pd(II) catalyst $[LPd(OH)_2]_2$ to form **RXT** by breaking the dinuclear reference state up into a mononuclear complex, subsequent rotations around Pd-O-B-C_{aryl} dihedrals result in two different pre-transmetalation intermediates where the ligand and aryl moiety are *cis* (**C**-prefixed structures) or *trans* (**T**-prefixed structures) to each other, respectively (**C1/T1**).

The aryl group undergoes transmetalation onto the palladium center (**C2/T2,** see **Supplementary Discussion S7.3** for details on the forms of **C2**), and H_2O subsequently displaces the $B(OH)_3$ ligand *via* nucleophilic substitution to form palladium-aqua complexes (**C3/T3**). Finally, intramolecular proton transfer from the coordinated water to the transmetalated *ipso*-carbon forms η^2-protoarene products (**C4/T4**), and facile protoarene dissociation regenerates the Pd(II) catalyst. Notably, the proton transfer and arene dissociation steps are formally the microscopic reverse of a concerted metalation deprotonation step in C-H activation.[48] In the following discussions, we broadly define "transmetalation" as the two steps involving intermediates **RXT, C1/T1** and **C2/T2,** and "proton transfer" as the two steps involving **C2/T2**, **C3/T3**, and **C4/T4**.
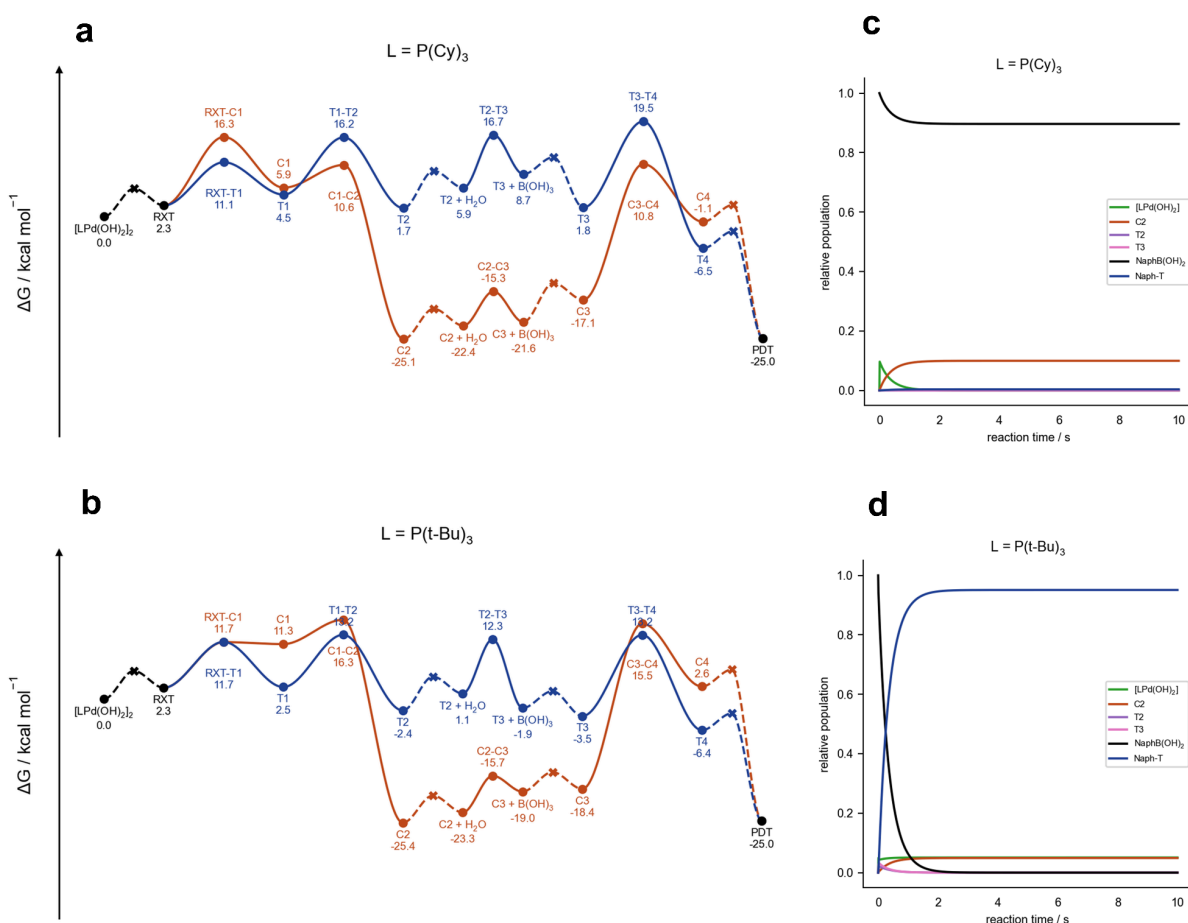
Figure 4: Computed reaction profiles for **a)** PCy_3 and **b)** $P(t\text{-Bu})_3$ for the proposed mechanism. ●: computed structures. ✖: Estimated transition state energies based on a 3.5 kcal/mol diffusion barrier at T = 333.15K (see **Computational Methods**). Relative population of key intermediates in the proposed mechanism from the kinetic model (**Supplementary Table S25**) for **c)** PCy_3 and **d)** $P(t\text{-Bu})_3$.

https://doi.org/10.26434/chemrxiv-2024-cw8cs-v2 **ORCID:** https://orcid.org/0000-0003-0597-5758 Content not peer-reviewed by ChemRxiv. **License:** CC BY-NC-ND 4.0

We note that the general form of the reaction profile is preserved across all 27 computed ligands (see **Supplementary Figures S97-S123**). Thus, we exemplify the analysis of the steric dependence of palladium-catalyzed PDB with PCy_3 (**Figure 4a**) and $P(t\text{-Bu})_3$ (**Figure 4b**), which experimentally showed negligible and significant PDB, respectively. The key difference in observed reactivity between ligands stems from the competition between the formation of catalytically inactive species in **C**-transmetalation versus the facile transmetalation and proton transfer processes in the **T**-pathway. This difference arises from the unstable **T**-transmetalation products **T2** and **T3,** as the ligands around the palladium center in these structures are arranged in a mutually *trans* soft-soft (phosphine and aryl) and hard-hard (⁻OH and OH_2 or BOH_3) fashion. In this arrangement, the soft ligands are unable to fully donate their electron densities to the palladium center as they compete to donate to the same metal d-orbital. This effect has previously been described as antisymbiotic destabilization.[49,50] Comparatively, **C2** and **C3** possess mutually *trans* soft-hard arrangements, allowing both soft ligands to fully contribute their electron density to the palladium center, making them very stable compared to their reference states.
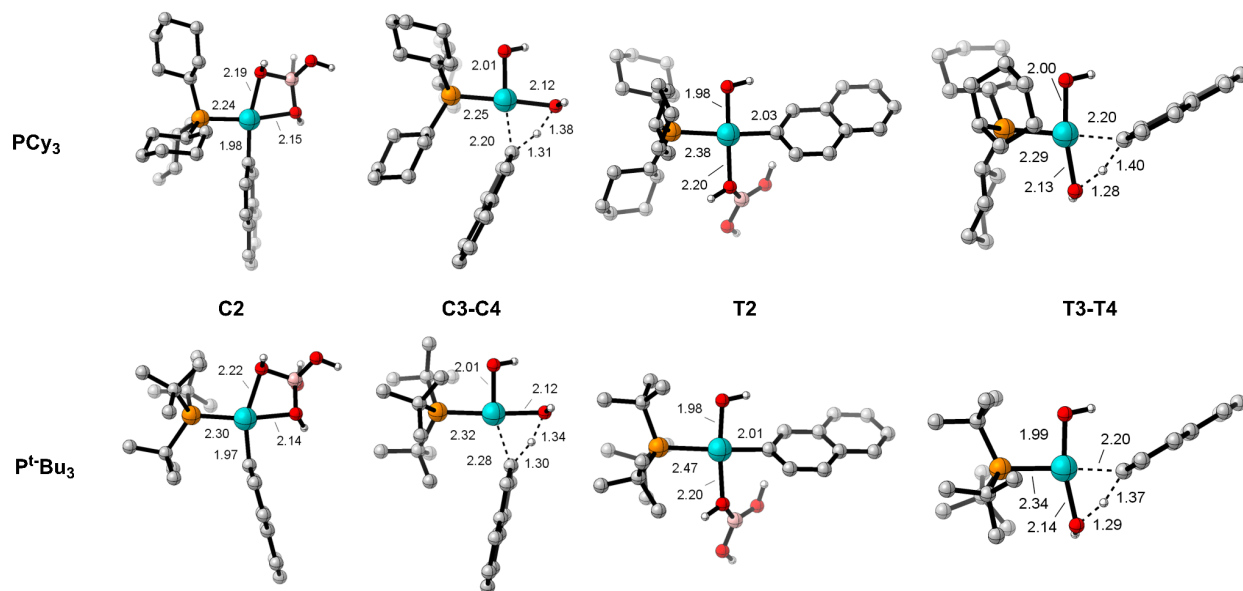

Figure 5: Key intermediates **C2** and **T2**, and transition states **C3-C4** and **T3-T4** for PCy_3 (top row) and $P(t\text{-Bu})_3$ (bottom row) with key bond lengths labeled in Angstroms (Å).

Both proton transfer transition states (**C3-C4** and **T3-T4**) transiently form unstable $[LPd(II)OH]^+$ structures as the R⁻ ligand dissociates in the proton transfer step, causing the electron density at the palladium center to decrease (**Figure 5**, see NBO[51] charges in **Supplementary Table S24**). In **T3-T4**, the electron density loss is less detrimental (**Supplementary Table S24**) as it is mitigated by the soft phosphine ligand *trans* to the partially dissociated R⁻, and, thus, accessing the **T3-T4** transition state from **T2** or **T3** is feasible, allowing for catalyst regeneration (19.4 and 16.8 kcal/mol for PCy_3 and $P(t\text{-Bu})_3$, respectively, **Figure 4a, 4b**). However, in **C3**-**C4,** the hard hydroxyl ligand *trans* to the partially dissociated R⁻ ligand is

unable to compensate for the loss in electron density, resulting in a large energetic barrier to access this transition state — PCy$_3$ and P(t-Bu)$_3$ require 35.9 and 39.8 kcal/mol, respectively, to surmount proton transfer barriers **C3-C4** (**Figure 4a, 4b**). Consequently, catalytic turnover only happens through the **T**-pathway. Ligands like PCy$_3$, which favor **C**-transmetalation over the **T**-pathway, will lead to the rapid population of stable species (**C2** or **C3**) and reduced **Naph** yields due to catalyst inactivity. In support of our proposed mechanism, we detected traces of a **C2** derivative for PCy$_3$ as a cation that is part of the boron"ate" complex [(2-Naph)Pd(PCy$_3$)]$^+$ = [R-Pd-L]$^+$ using HR-MS (**Supplementary Discussion S5.2**). We further propose that **C2** may also transmetalate with another molecule of a boronic acid derivative and, subsequently, undergo reductive elimination to yield binaphthalene, and Pd(0), which is inactive in PDB but essential for the SMC cycle (**Supplementary Discussion S7.8**).

In general, the nucleophilic substitution of B(OH)$_3$ by H$_2$O (**T2-T3**) is difficult as it requires a nucleophilic attack from a weak nucleophile (H$_2$O). The subsequent proton transfer to the coordinated naphthalene (**T3-T4**) is also difficult as palladium-aqua complexes are weak acids. We further note that the direct proton transfer from H$_2$O (**Supplementary Discussion S7.4**) or BOH$_3$ (**Supplementary Discussion S7.7.4**) onto the aryl moiety without nucleophilic substitution via **T2-T3** are both less energetically feasible than our proposed pathway. Hence, for significant PDB to occur, sufficient steric hindrance must be present to disfavor **C**-transmetalation and, in turn, favor the difficult post-transmetalation **T**-pathway steps. This preference can be described by an overall $\Delta\Delta G^\ddagger$ that accounts for the relative feasibility of catalyst trapping (**C**-transmetalation) versus catalytic PDB (**T**-pathway), computed as the difference between the maximum transition state Gibbs free energy of **C**-transmetalation (C$_{maxTM}$) and that of the entire **T**-pathway (T$_{max}$). In agreement with experimental observations, sterically compact ligands (phenyl, cyclohexyl) have relatively facile **RXT-C1** and **C1-C2** barriers that lead to quick catalyst poisoning and low **Naph** yields (brown and purple points, **Figure 6**). Phosphines with local steric bulk around the phosphorus atom (t-Bu or 1-adamantyl moieties) generally experience significant steric hindrance in *cis*-transmetalation **C1-C2** when the naphthalene moiety is forced closer to the phosphine ligand (orange points, **Figure 6**). This disfavours catalyst poisoning, leading to higher **Naph** yields. Finally, Buchwald ligands with compact alkyl substituents generally have elevated **RXT-C1** barriers, where the increased remote steric bulk from its biaryl moiety interferes with the dihedral rotation. However, such steric interference is less effective than for ligands with local steric bulk, ultimately leading to moderate **Naph** yields (blue points, **Figure 6**). The results of this analysis are consistent with the ligand-dependence identified in the experimental results (**Table 3**).

15
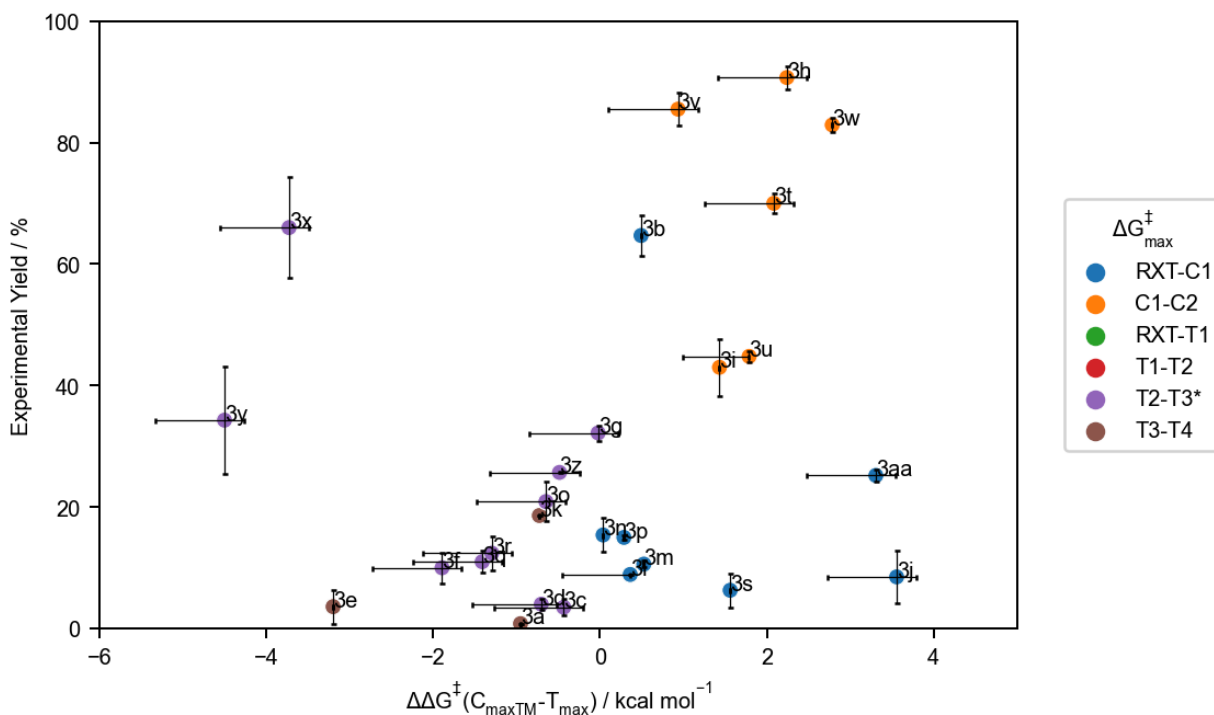
Figure 6: Experimental yield versus the free energy difference ($\Delta\Delta G^{\ddagger}$) between **C**-transmetalation (C_{maxTM}) and the entire **T**-pathway (T_{max}) for all 27 ligands at 3.5 eq [H_2O]. The vertical error bars denote the error in experimental yield (**Table 2**). The horizontal error bars denote how $\Delta\Delta G^{\ddagger}(C_{maxTM}-T_{max})$ is affected by changes to [H_2O] between 1.0 eq. (left bound) to 5.0 eq. (right bound). **T2-T3** barriers have a +2.59, +1.76, and +1.52 kcal/mol correction to account for the effects of [H_2O] at 1.0, 3.5 and 5.0 eq. respectively (**Supplementary Discussion S7.7.1**).

Kinetic modeling

To further validate our proposed mechanism, we constructed a kinetic model using *pykinetic*[52] and tracked the evolution of the intermediates and **Naph** over time (see **Supplementary Table S24** for the list of transformations in the kinetic model). We further distinguish between the two ways **Naph** can be made with a **-C** or **-T** suffix corresponding to the pathway that **Naph** is generated from. The kinetic campaign starts with the initial concentrations of [LPd(OH)$_2$]$_2$ = 0.001M and [NaphBOH$_2$] = 0.020M, following the experimental conditions used (see **Experimental Methods**), and 3.5 eq of H_2O ([H_2O] = 0.070M), an estimate obtained from the deuterium incorporation experiment. Across all ligands computed, we observe that there is no formation of **Naph-C** due to the formation of the thermodynamic trap **C2**, and thus the **T**-pathway is the only pathway that forms **Naph**. Ligands that have low **Naph-T** populations stem from the faster consumption of palladium to form **C2** (exemplified by PCy$_3$ in **Figure 4c**), limiting the extent of palladium-catalyzed PDB. Ligands that have high **Naph-T** populations also show significant populations of **C2** as the formation of **C2** is in general competitive with the formation of **Naph-T**. However, the extent

16

of palladium-catalyzed PDB is not constrained by the energetically disfavored **C**-pathway, resulting in significant PDB (exemplified by P(*t*-Bu)$_3$ in **Figure 4d**).

Assessing the validity of the proposed mechanism

We note that some ligands depart from the general trend observed for the relationship between experimental yield and $\Delta\Delta G^{\ddagger}$ (**Figure 6**), suggesting that it is possible that the ligand choice can affect the mechanism of palladium-catalyzed PDB. However, as the density functionals approximations contain intrinsic errors due to the approximations used to make computations tractable, and that the adventitious amounts of H$_2$O present may vary between experimental points, the selectivities between the **C-** and **T-** pathways are also subject to error, ultimately affecting the computational yields of **Naph-T**.

Simplified Two-Barrier Model
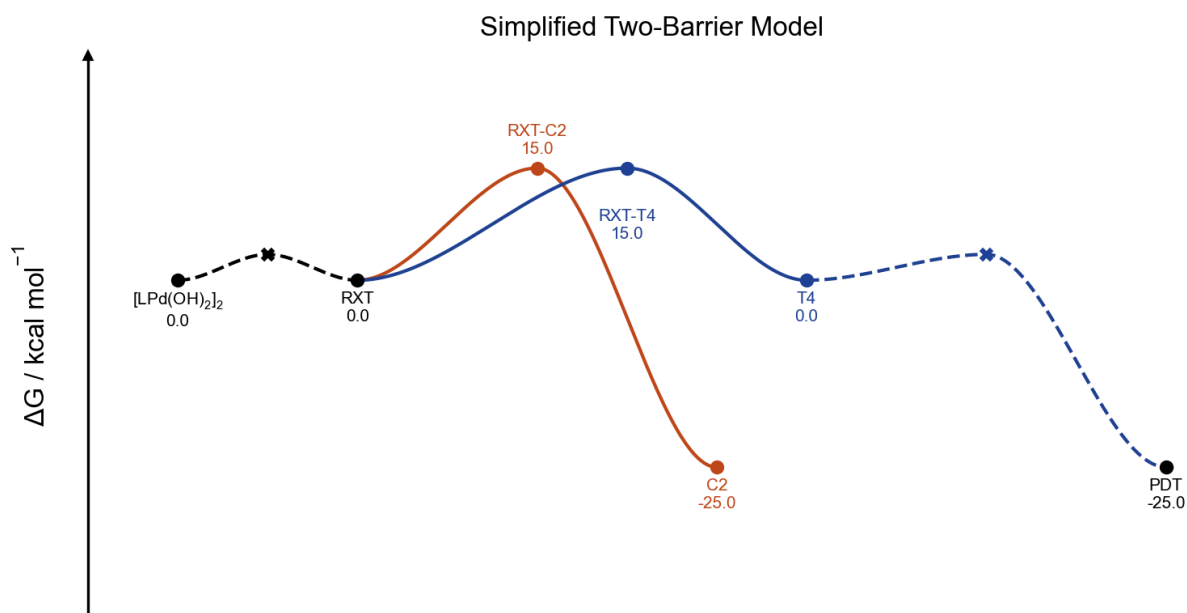
Figure 7: Reaction profile diagram for a simplified two-barrier model that aims to reproduce the full proposed mechanism.

In order to differentiate between the effects mentioned above, it is first necessary to determine the impact of the errors in each $\Delta G^{\ddagger}$ on the computed yield. However, evaluating the full mechanism requires the consideration of the errors of six transition state energies, leading to a large family of solutions that ultimately return the same $\Delta G^{\ddagger}$ and computed yield. Thus, we devise a simplified two-barrier model (**Figure 7**) defined by a single $\Delta\Delta G^{\ddagger}$ that is representative of our proposed mechanism. This model consists of a fictitious first-order "**RXT-C2**" catalyst trapping reaction and the H$_2$O-dependent "**RXT-T4**" PDB reaction (**Supplementary Table S25**). We then compare the computed yields from the full proposed mechanism to this simplified model, and record the $\Delta\Delta G^{\ddagger}$ required (presented as $\Delta\Delta G^{\ddagger}_{(RXT-C2-RXT-T4)}$ in **Figure 8**) for the simplified model to reproduce the yield from the full mechanism. We also record the

ΔΔG‡ required to reproduce the experimental yield, and plot that as the central sigmoidal line in **Figure 8**. In essence, the horizontal distance from a ligand's point in **Figure 8** to the central sigmoidal line signifies the amount ΔΔG‡ needs to change by in order for the computational yield in the simplified model to achieve parity with the experimental yield.

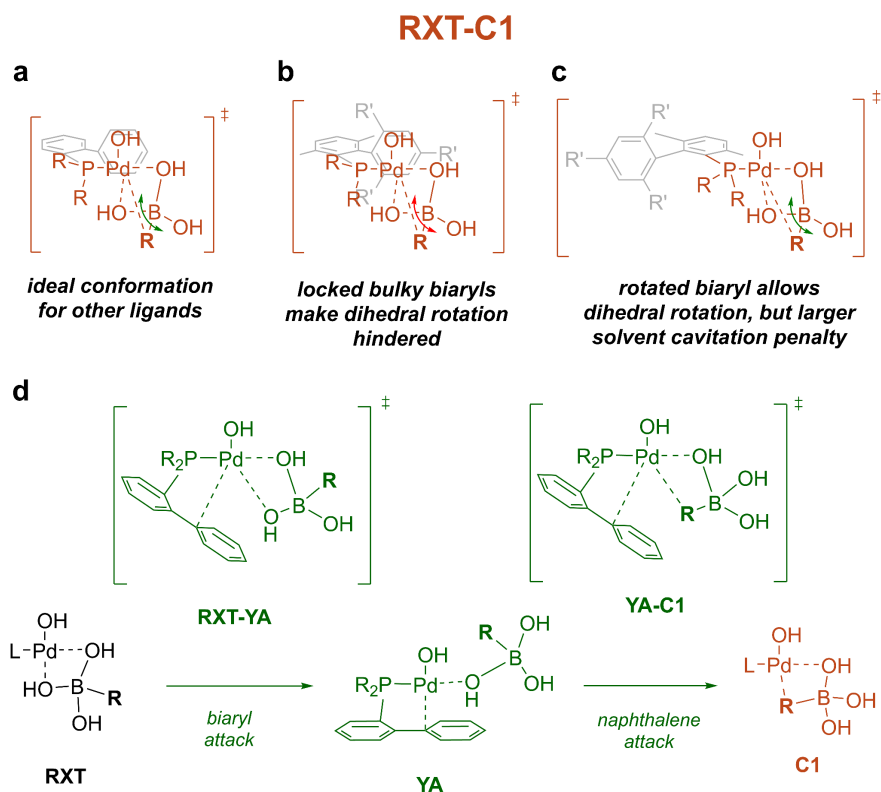With no prior assumption for the distribution of errors in the transition states, we calculate the change to ΔΔG‡ by assuming that both ΔG$^\ddagger_{RXT-C2}$ and ΔG$^\ddagger_{RXT-T4}$ must shift to the same extent and in opposite directions of each other, and that only the absolute energies of **RXT-C2** and **RXT-T4** shift. We denote this value as the *barrier tuning to parity prediction* metric. If the *barrier tuning to parity* prediction metric is below 1.0 kcal/mol (chemical accuracy, and the upper bound of performance of our method on benchmark reaction barrier height tasks),[53] denoted by the green shaded region in **Figure 8**, the mechanism is considered valid for the ligand considered. If the metric is larger than 1.0 kcal/mol (red shaded region in **Figure 8**), the proposed mechanism cannot reproduce the experimental yields within our defined bounds, suggesting that the proposed mechanism may not be correct for the ligand considered. We note that the conclusions based on this simplified model does not significantly affect the analysis below when compared to analyzing the full mechanism (**Supplementary Discussion S7.7.3**).

The above analysis based on the *barrier tuning to parity prediction* metric affords us the ability to identify ligands that may follow a separate mechanism. Gratifyingly, we observe that a majority (22 out of 27) of our ligands studied are able to reproduce the experimental yield within computational error bounds -- which is to have *barrier tuning to parity* prediction metrics of <±1.0 kcal/mol (**Figure 6**). In addition, we also plotted how computational yields are affected when [H_2O] is either 1.0 or 5.0 eq given that our estimates for [H_2O] could be subject to error. A minority of ligands (**3j, 3s, 3aa**) can reproduce the experimental yields within error bounds if [H_2O] is closer to 1.0 eq as opposed to the 3.5 eq estimate from our deuterium-incorporation experiments. Other ligands (**3x, 3y**) cannot reproduce the experimental yields even with higher [H_2O] equivalents, due to the fact that these ligands are characterized by an extremely high **T2-T3** barrier. We observe that conformationally-locked ligands (either with -OCH$_3$ or -Me groups on the aryl ring connected to the phosphorus atom) with immense remote steric bulk from the 2,4,6-tri-isopropylbenzene moiety (**3s, 3x, 3y, 3aa**) are poorly described by our mechanism.

18
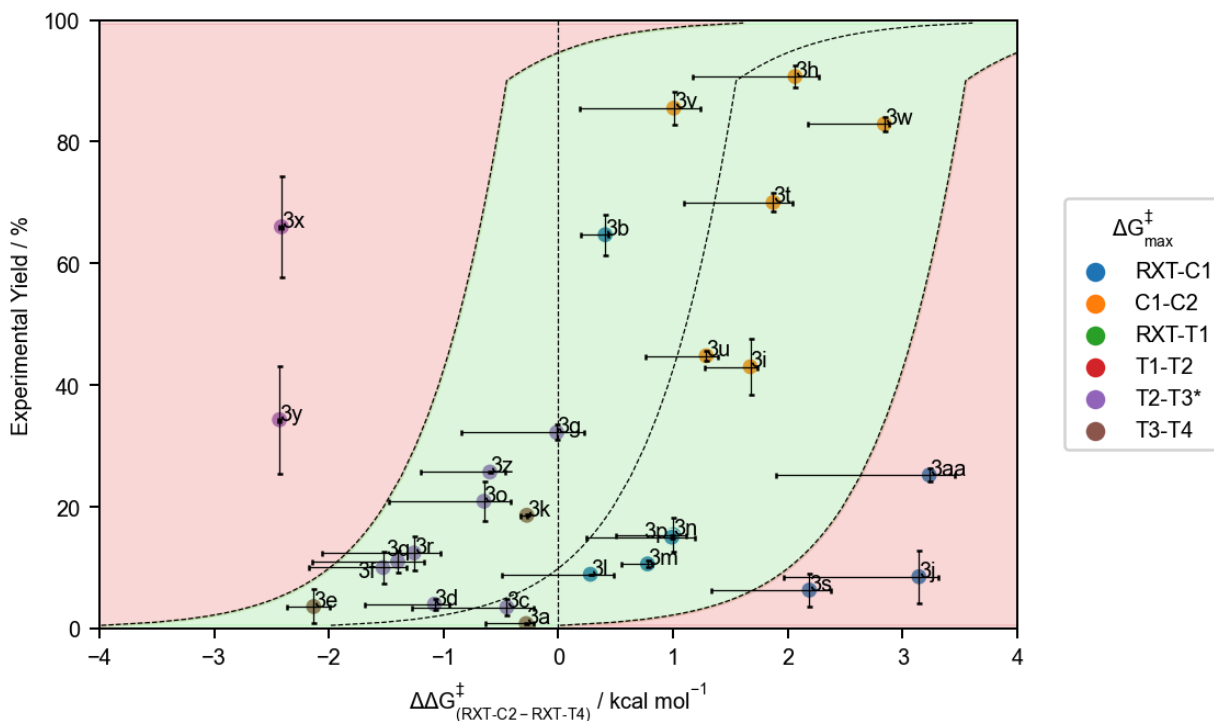
Figure 8: Experimental yield versus the free energy difference ($\Delta\Delta G^{\ddagger}$) in the simplified two-barrier model (**Figure 7**) that reproduces the computational yield at 3.5 eq [H_2O] of the full proposed mechanism for all 27 ligands. The vertical error bars denote the error in experimental yield (**Supplementary Discussion S3.1**), while the horizontal error bars denote the values of $\Delta\Delta G^{\ddagger}$ of the simplified model that reproduces the experimental yield when [H_2O] is 1.0 eq (left bound) and 5.0 eq (right bound). The central sigmoidal black dotted line denotes predicted computational yield for a given $\Delta\Delta G^{\ddagger}$ barrier for a simplified two-barrier model (**Supplementary Discussion S7.7.1**). Peripheral black dotted lines denote an error bound of ±2.0 kcal/mol for the simplified model's $\Delta\Delta G^{\ddagger}$, which corresponds to a *barrier tuning to parity prediction* metric of ±1.0 kcal/mol. Green and red shaded regions denote that the computed yields reproduce the experimental yields within, or outside the defined error bounds, respectively. The highest overall barrier amongst **C**-transmetalation and the **T**-pathway ($\Delta G^{\ddagger}_{max}$) in the full proposed mechanism computed for each ligand is color-coded in the legend, and **T2-T3** barriers have a +1.76 kcal/mol correction to account for the effects of [H_2O] (**Supplementary Discussion S7.7.1**).

19

Alternative mechanisms

RXT-C1

a ideal conformation for other ligands

b locked bulky biaryls make dihedral rotation hindered

c rotated biaryl allows dihedral rotation, but larger solvent cavitation penalty

d

RXT-YA

YA-C1

RXT → *biaryl attack* → YA → *naphthalene attack* → C1

Figure 9: Conformations for the **RXT-C1** transition states, and proposed alternative mechanism for the conversion of **RXT** to **C1** via **RXT-YA** and **YA-C1**.

We evaluate some alternative mechanistic propositions here, though we highlight in detail other possibilities for the poorly predicted ligands in **Supplementary Discussion S7.7.4** and **S7.7.5**. A full map of all considered mechanistic pathways can be found in **Supplementary Figure S45**. The anomalously high **Naph-T** computational yields for BrettPhos (**3s**) and AdBrettPhos (**3aa**) are due to high **RXT-C1** barriers (**Figure 10a, 10b**). The **RXT-C1** transition states for typical Buchwald ligands have the lowest energy conformer with the biaryl placed near the site of dihedral rotation (**Figure 9a**). However, in this conformation for BrettPhos and AdBrettPhos, the -OCH$_3$ moieties in the first phenyl of the biaryl force the tri-isopropyl-containing biaryl closer to the palladium center, making dihedral rotations of the naphthalene onto the palladium center extremely sterically hindered (**Figure 9b**). While the lowest energy conformer for BrettPhos was found to take the form in **Figure 9b**, we could not locate such a transition state for AdbrettPhos, and the lowest energy conformer found was one where the bulky biaryls are rotated away from the central palladium reaction core (**Figure 9c**).

20
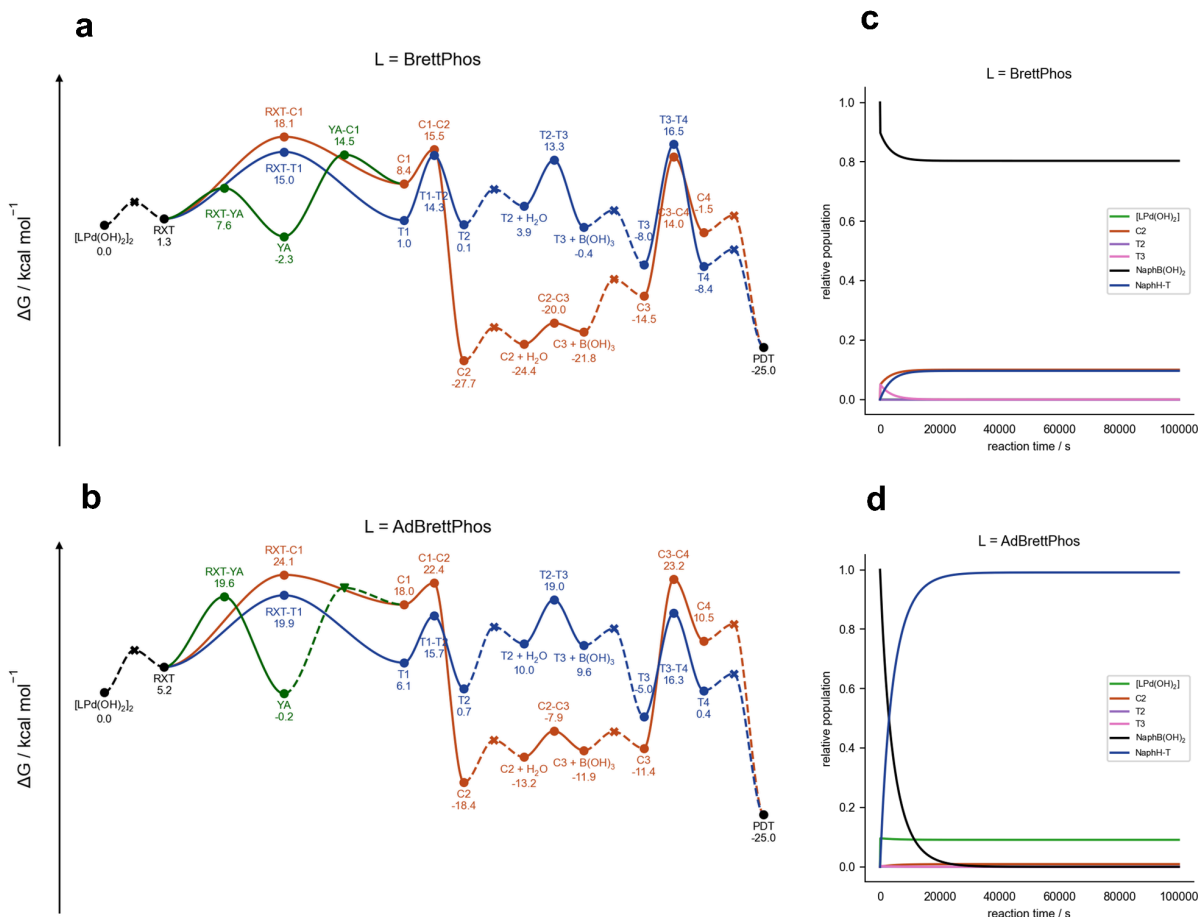
Figure 10: a-b) Computed reaction profiles for **a**) BrettPhos and **b**) AdBrettPhos with alternative mechanisms for forming **C1** included. ●: computed structures. ✖: Estimated transition state energies based on a 3.5 kcal/mol diffusion barrier at T = 333.15K (see **Computational Methods**). ▼: Transition state not found. **c-d)** Relative population of key intermediates in the proposed mechanism from the kinetic model (**Supplementary Table S28**) for **c**) BrettPhos and **d**) AdBrettPhos.

In our attempts to locate low-energy conformers for **RXT-C1** with our computational workflow, we found transition states where the tri-isopropyl biaryl attempts to displace either the hydroxyl group (**RXT-YA**) or the naphthalene group in a similar dihedral motion (**YA-C1**) (**Figure 9d**). The intermediate that forms from this process is **YA**, where the biaryl forms a η^2-coordination to palladium. The inclusion of **RXT-YA** and **YA-C1** for BrettPhos suppressed **Naph-T** yields down to 10%, in agreement with experimental yields (**Figure 10a, 10c**), and brings the *barrier tuning to parity* prediction down for BrettPhos down from -1.24 kcal/mol to -0.14 kcal/mol, We note that **RXT-C1** is still favored over the **YA** pathway for a series of other ligands we considered (**Supplementary Discussion S7.7.5**), suggesting that this mechanism may only be appropriate for BrettPhos. However, for AdBrettPhos, due to the steric bulk of the adamantyl moiety and the position assumed by the Buchwald biaryl in **YA**, the naphthalene moiety is not able to attack the palladium atom to form **C1**. As such, we were not able to locate a transition state for **YA-C1** (**Figure 10b**).

Even if the **YA** pathway was energetically more feasible than **RXT-C1**, AdBrettPhos still faces immense steric strain in the actual transmetalation event (**C1-C2**) where the 1-adamantyl moieties impede the approach of naphthalene for transmetalation, and, thus, the yields for AdBrettPhos remain poorly predicted (**Figure 10d**).

Correlation to ligand descriptors
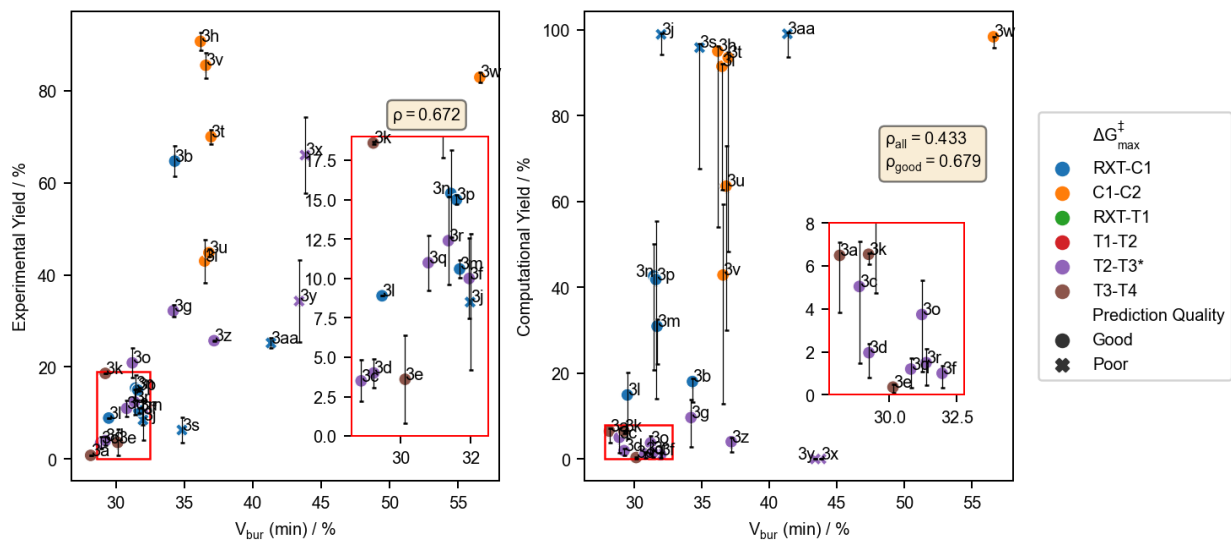
Figure 11: Pearson correlation plots of **a)** experimental yields and **b)** computational yields versus the percent buried volume of the ligand's minimum energy conformer (V_{bur} (min)). Prediction quality is considered good if the *barrier tuning to parity prediction* metric is <1.0 kcal/mol. Inset regions are marked in red. In all figures, a +1.76 kcal/mol correction is applied to the bimolecular reaction **T2-T3** to account for [H_2O] to compare first-order barriers on equal footing (**Supplementary Discussion S7.7.1**). The highest overall barrier amongst **C**-transmetalation and the **T**-pathway ($\Delta G^{\ddagger}_{max}$) computed for each ligand is color-coded in the legend.

Finally, we assess the correlation of the observed phenomena against pre-computed steric and electronic ligand properties in the monophosphine ligand database *kraken*.[54] We achieve decent Pearson *r* correlations between the percentage buried volume of the ligand's minimum energy conformer (V_{bur} (min)) against both experimental yields (ρ = 0.672) and the subset of well-predicted (**Figure 8,** within green bounds) computational yields (ρ = 0.679) (**Figure 11**). These results suggest that V_{bur} (min) can appropriately encapsulate both the effects of local and remote steric bulk of our set of phosphine ligands, providing a quick way to estimate the degree of PDB for new ligands. We note that higher correlations can be achieved with bespoke descriptors derived from buried volume (e.g. hemispheric or quadrant buried volumes, see **Supplementary Discussion S8**), but the small dataset we used in this study can lead to spurious correlations.

Conclusion

We demonstrated that bulky phosphine ligands can promote palladium-catalyzed protodeboronation under conditions relevant to the SMC. Furthermore, starting from Pd(0) sources like Pd_2dba_3 or Buchwald pre-catalysts that rapidly form Pd(0) instead of using $Pd(OAc)_2$ could help reduce unwanted protodeboronation in addition to minimizing catalyst initialization periods in SMC. This was observed experimentally under competitive cross-coupling and under conditions without the aryl halide, even when only adventitious water was present. Computational investigations revealed that bulky ligands favor the formation of a reactive post-transmetalation intermediate that, subsequently, undergoes facile proton transfer from water.

Adventitious water is challenging to avoid even with typical anhydrous conditions in organic synthesis, e.g., using anhydrous solvent and storing reagents in desiccators. Our results show that palladium-catalyzed protodeboronation with adventitious water can be a significant source of boronic reagent deactivation in cross-coupling conditions even with the increased resistance of boronic acid pinacol esters. This necessitates careful ligand selection for the SMC, especially in light of the trade-off between the ease of productive oxidative addition, transmetalation, and reductive elimination[18] versus the elevation of unproductive protodeboronation for bulky phosphines. In deciding the ligand for a new SMC synthetic protocol, we recommend consulting the buried volume of the ligand, which can be easily retrieved from the *kraken* database. Based on the ligands we evaluated, buried volumes below 33% show suppressed palladium-catalyzed protodeboronation and should provide greater selectivity for cross-coupled products in the SMC. Where possible, evaluating the full mechanistic pathway for the substrates and ligands of interest may also provide semi-quantitative yield predictions using kinetic modeling. As we have currently only demonstrated the ligand-dependence of palladium-catalyzed protodeboronation for electron-neutral boronic reagents, comprehensive studies towards the scope of aryl substituents and boronic moieties are required to gain a full understanding of palladium-catalyzed protodeboronation.

Methods

Experimental methods

Synthesis

Screening reactions were prepared by automatic solid weighing (+/- 2.5% limit) using the QUANTOS solid dosing platform for all palladium sources and ligands. Bases were subsequently dosed manually as the last reagent, either using a measuring scoop (K_3PO_4) or on an analytical balance (all bases in base screening, **Supplementary Discussion S3.4**), and the vials were capped immediately to avoid water absorption on base surface. The reactions were then performed on the high throughput reaction screening variant of the MEDUSA automation platform, including automated inert atmosphere handling, stock solution preparation, liquid dosing and heating/stirring, all controlled by Python code (see

Supplementary Discussion S2.1 for platform design and **Supplementary Discussion S2.2, S3.1-S3.4, S4.1-S4.3** for reaction details). All reactions were performed under an anhydrous N_2 atmosphere. All bases were stored under an anhydrous atmosphere and dried in an oven when necessary. 1,4-dioxane solvent from *Sure/Seal™* bottles was used, except for H_2O-loading experiments where a designated amount of H_2O was added to substrate stock solution quantitatively using a microsyringe. All experiments were at least duplicated. HPLC samples were prepared manually from the post-reaction mixtures and analyzed on an Agilent 1200 HPLC equipped with DAD, and the HPLC data (retention time, peak integration) were processed automatically using *python* code. Yield quantifications were performed based on calibration curves using independently synthesized or commercially available materials (see **Supplementary Discussion S1** for details).

Kinetic monitoring

Reagents for the kinetic monitoring procedure were prepared using the QUANTOS platform, and the procedure was performed on the continuous reaction monitoring variant of the MEDUSA automation platform. The automated reaction sampling and vial cleaning were synchronized with the Agilent 1200 HPLC running ChemStation using *python* code (see **Supplementary Discussion S4.1** for platform design, **Supplementary Discussion S4.2-S4.3** for reaction details, and the GitHub repository for platform control code). All experiments were at least duplicated. HPLC data were processed automatically using *python* code.

Computational methods

Density functional theory calculations

Structures were either automatically constructed through replacing phosphine ligands in previously manually-optimized JohnPhos (**3t**) structures *via kallisto*,[55] which handles post-replacement atomic clashes via GFN2-xTB[56] constrained optimization, or by manually replacing structural features in cases where the clash handling protocol gave incorrect structures. Conformer searches were subsequently conducted using CREST[57] with the GFN2-xTB semiempirical level of theory in the gas phase. The distances and angles around the palladium atoms were explicitly constrained to preserve square planar geometries and maintain the groups' relative arrangements around the palladium centers. In evaluating new conformers, transition state structures had key bond lengths additionally constrained based on previously DFT-optimized values. Single-point energy calculations for each optimized conformer were then evaluated at the PBE[58]-D3BJ[59,60]/def2-SVP[61] level of theory in the gas phase using Gaussian 16[62]. The lowest energy conformer identified by DFT was subsequently subjected to unconstrained geometry optimization and frequency calculations at the PBE-D3BJ/def2-SVP level of theory in the gas phase, with the W06 auxiliary basis set[63] for density fitting. Structures were ensured to have zero or one imaginary frequency if they are an intermediate or transition state, respectively. Single points were subsequently calculated using the DSD-PBEB95[64]-D3BJ/def2-QZVPP[61] level of theory with the auxiliary basis sets

24

def2/J,[63] def2-QZVPP/C,[65] and def2/JK,[66] incorporating implicit solvation in 1,4-dioxane (ε = 2.2099) with the SMD[67] model using ORCA 5.0.3.[68–72] The GoodVibes[73] package was used to apply quasi-harmonic approximations for frequency calculations *via* the Truhlar scheme[74] at 333.15 K, with solution-phase standard state corrections and entropic corrections concerning symmetry.

Kinetic modeling

The kinetic models were constructed with the *pykinetic* package.[52] The energies of each reactant and intermediate are provided in one file, while the possible reactions that are allowed in the kinetic model are specified in another file with the energies of the transition state provided for each reaction. All reactions are treated as reversible, and the forward and backward reaction rates are calculated as $(\kappa k_b T/h)exp(-E_a/RT)$, where k_b is the Boltzmann constant 1.381×10^{-23} J$\cdot$K^{-1}, h is the Planck constant 6.626×10^{-34} kg$\cdot$m$^2\cdot$s^{-1}, E_a is the activation energy specified in J/mol, R is the gas constant 8.314 J mol$^{-1}\cdot$K^{-1}, and T is the reaction temperature, specified to be 333.15 K. The transmission coefficient κ is assumed to be 1. The forward and backward activation energies are provided as the differences between the transition state energies and the sum of reactant energies or product energies respectively. The rate of change of each tracked intermediate is expressed as a sum of the rates of reactions that produce and consume the intermediate, and is solved as a system of ordinary differential equations. We used the *scipy v1.9.3*[75] bindings for the LSODA numerical solver, which is part of the ODEPACK[76] package. The absolute and relative tolerance parameters for LSODA were defined as 10^{-7} and 10^{-12}, respectively.

Associative and dissociative processes (**Supplementary Table S25**, reactions 1, 2, 7, 12, for example) do not have transition states calculated and are assumed to be diffusion-limited.[77] The specification of a barrier is necessary to ensure numerical stability in the kinetic model when rates are extremely high due to very small energy differences. The diffusion constant was calculated using the formula proposed by Rush et al.,[78] incorporating a viscosity constant η with a value of $2.09\cdot10^{-7}$ P$\cdot$s for 1,4-dioxane.[79] Given the temperature of 333.15K, the diffusion barrier is estimated to be 3.46 kcal/mol, and the transition state energies specified for diffusion-limited reactions are calculated from the highest of either the reactant or product energies specified.

The initial concentrations were set to $[LPd(OH)_2]_2$ = 0.001M and $[NaphBOH_2]$ = 0.020M following the experimental conditions used (**Supplementary Discussion S2.2**), and $[H_2O]$ = 0.070M (3.5 eq) as an estimate from deuterium incorporation, where 20 equivalents of added D_2O resulted in 83% deuterodeboronated product and 17% of protodeboronated product (**Supplementary Discussion S5.1**). We note that we model the dissociation of $[LPd(OH)_2]_2$ to form two equivalents of $[LPd(OH)_2]$ as diffusion-limited, and the initial concentration of $[LPd(OH)_2]_2$ provided will generate the correct 10 mol% of catalyst in the kinetic model. The products we track are $B(OH)_3$ and **Naph**, which is split into **Naph-C** and **Naph-T** to illustrate the two ways **Naph** can be formed from the **C-** and **T**-pathways respectively. **Naph-C**

is not depicted in the kinetic model traces as the **C3-C4** transition states are insurmountable in the timescales of the kinetic model. We also track the reaction intermediates **C2**, **T2** and **T3** as they can be more stable than the starting reactant state (depending on the ligand) and build up a significant population. As *pykinetic* requires that the duration of the kinetic modeling be specified before the populations are allowed to evolve, the end time for each ligand was determined to be the point where the populations do not change significantly anymore with time. LSODA adaptively adjusts the time step based on the problem's dynamics, and we have found that the product distributions remain consistent regardless of the solver's step-size adjustments.

Statistical analysis

Pearson correlation analysis between *kraken* descriptors and experimental and computational yields were performed using *scipy v1.9.3*.[75]

Data Availability

All code for experimental hardware manipulation, experimental data extraction, analyze computational output, and plot figures are available on GitHub at https://github.com/chertianser/pdcatpdb-code and on Zenodo at https://doi.org/10.5281/zenodo.13246410. All code used by and generated by *pykinetic* are also available on GitHub and Zenodo. All computed structures and single points are available on https://iochem-bd.matter.toronto.edu.

Author Contributions

C.T.S. and H.H. contributed equally to the work. C.T.S., H.H., R.P. and A.A.-G. conceptualized the work. C.T.S. performed the computational mechanistic analysis, including the calculation of all structures and kinetic models. H.H. and S.L. performed the experiments, and H.H. performed all characterizations and analysis of experimental results. C.T.S., R.P. and K.J. co-designed the computational workflow for structural generation. C.T.S. and S.P.-G. co-designed the workflow for constructing kinetic models. H.H., S.L., and R.P. co-designed the experiments and protocols. All authors discussed the results, analyzed the data, and contributed to the writing and proofreading of the manuscript.

References

(1) Miyaura, N.; Suzuki, A. Palladium-Catalyzed Cross-Coupling Reactions of Organoboron Compounds. *Chem. Rev.* **1995**, *95* (7), 2457–2483.

(2) Johansson Seechurn, C. C. C.; Kitching, M. O.; Colacot, T. J.; Snieckus, V. Palladium-Catalyzed Cross-Coupling: A Historical Contextual Perspective to the 2010 Nobel Prize. *Angew. Chem. Int. Ed.* **2012**, *51* (21), 5062–5085. https://doi.org/10.1002/anie.201107017.

(3) Cooper, T. W. J.; Campbell, I. B.; Macdonald, S. J. F. Factors Determining the Selection of Organic Reactions by Medicinal Chemists and the Use of These Reactions in Arrays (Small Focused Libraries). *Angew. Chem. Int. Ed.* **2010**, *49* (44), 8082–8091. https://doi.org/10.1002/anie.201002238.

(4) Brown, D. G.; Boström, J. Analysis of Past and Present Synthetic Methodologies on Medicinal Chemistry: Where Have All the New Reactions Gone? *J. Med. Chem.* **2016**, *59* (10), 4443–4458. https://doi.org/10.1021/acs.jmedchem.5b01409.

(5) Kuivila, H. G.; Reuwer Jr., J. F.; Mangravite, J. A. ELECTROPHILIC DISPLACEMENT REACTIONS: XV. KINETICS AND MECHANISM OF THE BASE-CATALYZED PROTODEBORONATION OF ARENEBORONIC ACIDS. *Can. J. Chem.* **1963**, *41* (12), 3081–3090. https://doi.org/10.1139/v63-451.

(6) Kuivila, H. G.; Reuwer, J. F.; Mangravite, J. A. Electrophilic Displacement Reactions. XVI. Metal Ion Catalysis in the Protodeboronation of Areneboronic Acids1-3. *J. Am. Chem. Soc.* **1964**, *86* (13), 2666–2670. https://doi.org/10.1021/ja01067a031.

(7) Kuivila, H. G.; Reuwer Jr, J. F.; Mangravite, J. A. Electrophilic Displacement Reactions: XV. Kinetics and Mechanism of the Base-Catalyzed Protodeboronation of Areneboronic Acids. *Can. J. Chem.* **1963**, *41* (12), 3081–3090.

(8) Kuivila, H. G.; Nahabedian, K. V. Electrophilic Displacement Reactions. X. General Acid Catalysis in the Protodeboronation of Areneboronic Acids1-3. *J. Am. Chem. Soc.* **1961**, *83* (9), 2159–2163.

(9) Shen, F.; Tyagarajan, S.; Perera, D.; Krska, S. W.; Maligres, P. E.; Smith, M. R.; Maleczka, R. E. Bismuth Acetate as a Catalyst for the Sequential Protodeboronation of Di- and Triborylated Indoles. *Org. Lett.* **2016**, *18* (7), 1554–1557. https://doi.org/10.1021/acs.orglett.6b00356.

(10) Loach, R. P.; Fenton, O. S.; Amaike, K.; Siegel, D. S.; Ozkal, E.; Movassaghi, M. C7-Derivatization of C3-Alkylindoles Including Tryptophans and Tryptamines. *J. Org. Chem.* **2014**, *79* (22), 11254–11263. https://doi.org/10.1021/jo502062z.

(11) Kallepalli, V. A.; Gore, K. A.; Shi, F.; Sanchez, L.; Chotana, G. A.; Miller, S. L.; Maleczka, R. E. Jr.; Smith, M. R. I. Harnessing C–H Borylation/Deborylation for Selective Deuteration, Synthesis of Boronate Esters, and Late Stage Functionalization. *J. Org. Chem.* **2015**, *80* (16), 8341–8353. https://doi.org/10.1021/acs.joc.5b01588.

(12) Sadler, S. A.; Hones, A. C.; Roberts, B.; Blakemore, D.; Marder, T. B.; Steel, P. G. Multidirectional Synthesis of Substituted Indazoles via Iridium-Catalyzed C–H Borylation. *J. Org. Chem.* **2015**, *80* (10), 5308–5314. https://doi.org/10.1021/acs.joc.5b00452.

(13) Nave, S.; Sonawane, R. P.; Elford, T. G.; Aggarwal, V. K. Protodeboronation of Tertiary Boronic Esters: Asymmetric Synthesis of Tertiary Alkyl Stereogenic Centers. *J. Am. Chem. Soc.* **2010**, *132* (48), 17096–17098. https://doi.org/10.1021/ja1084207.

(14) Rasappan, R.; Aggarwal, V. K. Synthesis of Hydroxyphthioceranic Acid Using a Traceless Lithiation–Borylation–Protodeboronation Strategy. *Nat. Chem.* **2014**, *6* (9), 810–814. https://doi.org/10.1038/nchem.2010.

(15) Cox, P. A.; Leach, A. G.; Campbell, A. D.; Lloyd-Jones, G. C. Protodeboronation of Heteroaromatic, Vinyl, and Cyclopropyl Boronic Acids: pH–Rate Profiles, Autocatalysis, and Disproportionation. *J. Am. Chem. Soc.* **2016**, *138* (29), 9145–9157. https://doi.org/10.1021/jacs.6b03283.

(16) Cox, P. A.; Reid, M.; Leach, A. G.; Campbell, A. D.; King, E. J.; Lloyd-Jones, G. C. Base-Catalyzed Aryl-B (OH) 2 Protodeboronation Revisited: From Concerted Proton Transfer to Liberation of a Transient Aryl Anion. *J. Am. Chem. Soc.* **2017**, *139* (37), 13156–13165. https://doi.org/10.1021/jacs.7b07444.

(17) Hayes, H. L.; Wei, R.; Assante, M.; Geogheghan, K. J.; Jin, N.; Tomasi, S.; Noonan, G.; Leach, A. G.; Lloyd-Jones, G. C. Protodeboronation of (Hetero) Arylboronic Esters: Direct versus Prehydrolytic Pathways and Self-/Auto-Catalysis. *J. Am. Chem. Soc.* **2021**, *143* (36), 14814–14826. https://doi.org/10.1021/jacs.1c06863.

(18) Martin, R.; Buchwald, S. L. Palladium-Catalyzed Suzuki−Miyaura Cross-Coupling Reactions Employing Dialkylbiaryl Phosphine Ligands. *Acc. Chem. Res.* **2008**, *41* (11), 1461–1473. https://doi.org/10.1021/ar800036s.

(19) Barder, T. E.; Walker, S. D.; Martinelli, J. R.; Buchwald, S. L. Catalysts for Suzuki−Miyaura Coupling Processes: Scope and Studies of the Effect of Ligand Structure. *J. Am. Chem. Soc.* **2005**, *127* (13), 4685–4696. https://doi.org/10.1021/ja042491j.

(20) Lennox, A. J.; Lloyd-Jones, G. C. Selection of Boron Reagents for Suzuki–Miyaura Coupling. *Chem. Soc. Rev.* **2014**, *43* (1), 412–443.

(21) Florentin, D.; Fournié-Zaluski, M. C.; Callanquin, M.; Roques, B. P. Etude Des pK $_a$ et de La Protodéboronation Des Acides Furanneboroniques. *J. Heterocycl. Chem.* **1976**, *13* (6), 1265–1272. https://doi.org/10.1002/jhet.5570130624.

(22) Liu, C.; Li, X.; Wu, Y.; Qiu, J. Copper-Catalyzed Protodeboronation of Arylboronic Acids in Aqueous Media. *RSC Adv.* **2014**, *4* (97), 54307–54311. https://doi.org/10.1039/C4RA11659C.

(23) Barker, G.; Webster, S.; Johnson, D. G.; Curley, R.; Andrews, M.; Young, P. C.; Macgregor, S. A.; Lee, A.-L. Gold-Catalyzed Proto-and Deuterodeboronation. *J. Org. Chem.* **2015**, *80* (20), 9807–9816. https://doi.org/10.1021/acs.joc.5b01041.

(24) Li, N.; Xiong, F.; Gao, K. Cobalt-Catalyzed Protodeboronation of Aryl and Vinyl Boronates. *J. Org. Chem.* **2021**, *86* (2), 1972–1979. https://doi.org/10.1021/acs.joc.0c02570.

(25) Liu, C.; Li, X.; Wu, Y. Base-Promoted Silver-Catalyzed Protodeboronation of Arylboronic Acids and Esters. *RSC Adv.* **2015**, *5* (20), 15354–15358.

(26) Partyka, D. V. Transmetalation of Unsaturated Carbon Nucleophiles from Boron-Containing Species to the Mid to Late d-Block Metals of Relevance to Catalytic C−X Coupling Reactions (X = C, F, N, O, Pb, S, Se, Te). *Chem. Rev.* **2011**, *111* (3), 1529–1595. https://doi.org/10.1021/cr1002276.

(27) Strieth-Kalthoff, F.; Hao, H.; Rathore, V.; Derasp, J.; Gaudin, T.; Angello, N. H.; Seifrid, M.; Trushina, E.; Guy, M.; Liu, J.; Tang, X.; Mamada, M.; Wang, W.; Tsagaantsooj, T.; Lavigne, C.; Pollice, R.; Wu, T. C.; Hotta, K.; Bodo, L.; Li, S.; Haddadnia, M.; Wołos, A.; Roszak, R.; Ser, C. T.; Bozal-Ginesta, C.; Hickman, R. J.; Vestfrid, J.; Aguilar-Granda, A.; Klimareva, E. L.; Sigerson, R. C.; Hou, W.; Gahler, D.; Lach, S.; Warzybok, A.; Borodin, O.; Rohrbach, S.; Sanchez-Lengeling, B.; Adachi, C.; Grzybowski, B. A.; Cronin, L.; Hein, J. E.; Burke, M. D.; Aspuru-Guzik, A. Delocalized, Asynchronous, Closed-Loop Discovery of Organic Laser Emitters. *Science* **2024**, *384* (6697), eadk9227. https://doi.org/10.1126/science.adk9227.

(28) Angello, N. H.; Rathore, V.; Beker, W.; Wołos, A.; Jira, E. R.; Roszak, R.; Wu, T. C.; Schroeder, C. M.; Aspuru-Guzik, A.; Grzybowski, B. A.; Burke, M. D. Closed-Loop Optimization of General Reaction Conditions for Heteroaryl Suzuki-Miyaura Coupling. *Science* **2022**, *378* (6618), 399–405. https://doi.org/10.1126/science.adc8743.

(29) Pablo-García, S.; García, Á.; Akkoc, G. D.; Sim, M.; Cao, Y.; Somers, M.; Hattrick, C.; Yoshikawa, N.; Dworschak, D.; Hao, H.; Aspuru-Guzik, A. An Affordable Platform for Automated Synthesis and Electrochemical Characterization. ChemRxiv February 9, 2024. https://doi.org/10.26434/chemrxiv-2024-cwnwc.

(30) Sim, M.; Vakili, M. G.; Strieth-Kalthoff, F.; Hao, H.; Hickman, R. J.; Miret, S.; Pablo-García, S.; Aspuru-Guzik, A. ChemOS 2.0: An Orchestration Architecture for Chemical Self-Driving Laboratories. *Matter* **2024**, *7* (9), 2959–2977. https://doi.org/10.1016/j.matt.2024.04.022.

(31) Carrow, B. P.; Hartwig, J. F. Distinguishing Between Pathways for Transmetalation in Suzuki−Miyaura Reactions. *J. Am. Chem. Soc.* **2011**, *133* (7), 2116–2119. https://doi.org/10.1021/ja1108326.

(32) Amatore, C.; Jutand, A.; Le Duc, G. Kinetic Data for the Transmetalation/Reductive Elimination in Palladium-Catalyzed Suzuki-Miyaura Reactions: Unexpected Triple Role of Hydroxide Ions Used as Base. *Chem. - Eur. J.* **2011**, *17* (8), 2492–2503. https://doi.org/10.1002/chem.201001911.

(33) Adamo, C.; Amatore, C.; Ciofini, I.; Jutand, A.; Lakmini, H. Mechanism of the Palladium-Catalyzed Homocoupling of Arylboronic Acids: Key Involvement of a Palladium Peroxo Complex. *J. Am.*

Chem. Soc. **2006**, *128* (21), 6829–6836. https://doi.org/10.1021/ja0569959.

(34) Shi, Y.; Derasp, J. S.; Maschmeyer, T.; Hein, J. E. Phase Transfer Catalysts Shift the Pathway to Transmetalation in Biphasic Suzuki-Miyaura Cross-Couplings. *Nat. Commun.* **2024**, *15* (1), 5436. https://doi.org/10.1038/s41467-024-49681-4.

(35) Zhang, H. C.; Daves, G. D. Jr. Water Facilitation of Palladium-Mediated Coupling Reactions. *Organometallics* **1993**, *12* (5), 1499–1500. https://doi.org/10.1021/om00029a005.

(36) Kuivila, H. G.; Reuwer, J. F.; Mangravite, J. A. Electrophilic Displacement Reactions. XVI. Metal Ion Catalysis in the Protodeboronation of Areneboronic Acids1-3. *J. Am. Chem. Soc.* **1964**, *86* (13), 2666–2670. https://doi.org/10.1021/ja01067a031.

(37) Amatore, C.; Jutand, A.; M'Barki, M. A. Evidence of the Formation of Zerovalent Palladium from Pd (OAc) 2 and Triphenylphosphine. *Organometallics* **1992**, *11* (9), 3009–3013. https://doi.org/10.1021/om00045a012.

(38) Amatore, C.; Jutand, A.; Thuilliez, A. Formation of Palladium(0) Complexes from Pd(OAc)2 and a Bidentate Phosphine Ligand (Dppp) and Their Reactivity in Oxidative Addition. *Organometallics* **2001**, *20* (15), 3241–3249. https://doi.org/10.1021/om0101137.

(39) McLaughlin, P. A.; Verkade, J. G. Fluoride-Catalyzed Reduction of Palladium(II) to Palladium(0)−Phosphine Complexes. *Organometallics* **1998**, *17* (26), 5937–5940. https://doi.org/10.1021/om980490s.

(40) Adamo, C.; Amatore, C.; Ciofini, I.; Jutand, A.; Lakmini, H. Mechanism of the Palladium-Catalyzed Homocoupling of Arylboronic Acids: Key Involvement of a Palladium Peroxo Complex. *J. Am. Chem. Soc.* **2006**, *128* (21), 6829–6836. https://doi.org/10.1021/ja0569959.

(41) Yoshida, H.; Yamaryo, Y.; Ohshita, J.; Kunai, A. Base-Free Oxidative Homocoupling of Arylboronic Esters. *Tetrahedron Lett.* **2003**, *44* (8), 1541–1544. https://doi.org/10.1016/S0040-4039(03)00023-6.

(42) Amatore, C.; Carre, E.; Jutand, A.; M'Barki, M. A. Rates and Mechanism of the Formation of Zerovalent Palladium Complexes from Mixtures of Pd (OAc) 2 and Tertiary Phosphines and Their Reactivity in Oxidative Additions. *Organometallics* **1995**, *14* (4), 1818–1826. https://doi.org/10.1021/om00004a039.

(43) Thomas, A. A.; Wang, H.; Zahrt, A. F.; Denmark, S. E. Structural, Kinetic, and Computational Characterization of the Elusive Arylpalladium (II) Boronate Complexes in the Suzuki–Miyaura Reaction. *J. Am. Chem. Soc.* **2017**, *139* (10), 3805–3821. https://doi.org/10.1021/jacs.6b13384.

(44) Pollice, R.; Schnürch, M. Investigations into the Kinetic Modeling of the Direct Alkylation of Benzylic Amines: Dissolution of K2CO3 Is Responsible for the Observation of an Induction Period. *J. Org. Chem.* **2015**, *80* (16), 8268–8274. https://doi.org/10.1021/acs.joc.5b01335.

(45) Nielsen, M. M.; Pedersen, C. M. Vessel Effects in Organic Chemical Reactions; a Century-Old, Overlooked Phenomenon. *Chem. Sci.* **2022**, *13* (21), 6181–6196. https://doi.org/10.1039/D2SC01125E.

(46) Thomas, A. A.; Zahrt, A. F.; Delaney, C. P.; Denmark, S. E. Elucidating the Role of the Boronic

Esters in the Suzuki–Miyaura Reaction: Structural, Kinetic, and Computational Investigations. *J. Am. Chem. Soc.* **2018**, *140* (12), 4401–4416. https://doi.org/10.1021/jacs.8b00400.

(47) Thomas, A. A.; Denmark, S. E. Pre-Transmetalation Intermediates in the Suzuki-Miyaura Reaction Revealed: The Missing Link. *Science* **2016**, *352* (6283), 329–332. https://doi.org/10.1126/science.aad6981.

(48) Lapointe, D.; Fagnou, K. Overview of the Mechanistic Work on the Concerted Metallation–Deprotonation Pathway. *Chem. Lett.* **2010**, *39* (11), 1118–1126. https://doi.org/10.1246/cl.2010.1118.

(49) Pearson, R. G. Antisymbiosis and the Trans Effect. *Inorg. Chem.* **1973**, *12* (3), 712–713. https://doi.org/10.1021/ic50121a052.

(50) Vicente, J.; Arcas, A.; Bautista, D.; Jones, P. G. The Difficulty of Coordinating Mutually Trans Phosphine and Aryl Ligands in Palladium Complexes and Its Relation to Important Coupling Processes. Syntheses and Crystal Structures of a Family of Palladium Phosphino, Triflato, Perchlorato, and Aquo-2-(Arylazo)Aryl Complexes. *Organometallics* **1997**, *16* (10), 2127–2138. https://doi.org/10.1021/om961094h.

(51) Glendening, E. D.; Landis, C. R.; Weinhold, F. NBO 7.0: New Vistas in Localized and Delocalized Chemical Bonding Theory. *J. Comput. Chem.* **2019**, *40* (25), 2234–2241. https://doi.org/10.1002/jcc.25873.

(52) Pérez-Soto, R.; Pablo-García, S.; Besora, M.; Maseras, F. Rperezsoto/Pykinetic: V0.1.0, 2023. https://doi.org/10.5281/zenodo.8053050.

(53) Goerigk, L.; Hansen, A.; Bauer, C.; Ehrlich, S.; Najibi, A.; Grimme, S. A Look at the Density Functional Theory Zoo with the Advanced GMTKN55 Database for General Main Group Thermochemistry, Kinetics and Noncovalent Interactions. *Phys. Chem. Chem. Phys.* **2017**, *19* (48), 32184–32215. https://doi.org/10.1039/C7CP04913G.

(54) Gensch, T.; dos Passos Gomes, G.; Friederich, P.; Peters, E.; Gaudin, T.; Pollice, R.; Jorner, K.; Nigam, A.; Lindner-D'Addario, M.; Sigman, M. S. A Comprehensive Discovery Platform for Organophosphorus Ligands for Catalysis. *J. Am. Chem. Soc.* **2022**, *144* (3), 1205–1217. https://doi.org/10.1021/jacs.1c09718.

(55) Caldeweyher, E. Kallisto: A Command-Line Interface to Simplify Computational Modelling and the Generation of Atomic Features. *J. Open Source Softw.* **2021**, *6* (60), 3050.

(56) Bannwarth, C.; Ehlert, S.; Grimme, S. GFN2-xTB—An Accurate and Broadly Parametrized Self-Consistent Tight-Binding Quantum Chemical Method with Multipole Electrostatics and Density-Dependent Dispersion Contributions. *J. Chem. Theory Comput.* **2019**, *15* (3), 1652–1671. https://doi.org/10.1021/acs.jctc.8b01176.

(57) Pracht, P.; Bohle, F.; Grimme, S. Automated Exploration of the Low-Energy Chemical Space with Fast Quantum Chemical Methods. *Phys. Chem. Chem. Phys.* **2020**, *22* (14), 7169–7192. https://doi.org/10.1039/C9CP06869D.

(58) Perdew, J. P.; Burke, K.; Ernzerhof, M. Generalized Gradient Approximation Made Simple. *Phys. Rev. Lett.* **1996**, *77* (18), 3865. https://doi.org/10.1103/PhysRevLett.77.3865.

(59) Grimme, S.; Ehrlich, S.; Goerigk, L. Effect of the Damping Function in Dispersion Corrected Density Functional Theory. *J. Comput. Chem.* **2011**, *32* (7), 1456–1465. https://doi.org/10.1002/jcc.21759.

(60) Grimme, S.; Antony, J.; Ehrlich, S.; Krieg, H. A Consistent and Accurate Ab Initio Parametrization of Density Functional Dispersion Correction (DFT-D) for the 94 Elements H-Pu. *J. Chem. Phys.* **2010**, *132* (15). https://doi.org/10.1063/1.3382344.

(61) Weigend, F.; Ahlrichs, R. Balanced Basis Sets of Split Valence, Triple Zeta Valence and Quadruple Zeta Valence Quality for H to Rn: Design and Assessment of Accuracy. *Phys. Chem. Chem. Phys.* **2005**, *7* (18), 3297–3305.

(62) Frisch, M. J.; Trucks, G. W.; Schlegel, H. B.; Scuseria, G. E.; Robb, M. A.; Cheeseman, J. R.; Scalmani, G.; Barone, V.; Petersson, G. A.; Nakatsuji, H. *Gaussian 16*; Gaussian, Inc. Wallingford, CT, 2016.

(63) Weigend, F. Accurate Coulomb-Fitting Basis Sets for H to Rn. *Phys. Chem. Chem. Phys.* **2006**, *8* (9), 1057–1065. https://doi.org/10.1039/B515623H.

(64) Kozuch, S.; Martin, J. M. L. Spin-Component-Scaled Double Hybrids: An Extensive Search for the Best Fifth-Rung Functionals Blending DFT and Perturbation Theory. *J. Comput. Chem.* **2013**, *34* (27), 2327–2344. https://doi.org/10.1002/jcc.23391.

(65) Hellweg, A.; Hättig, C.; Höfener, S.; Klopper, W. Optimized Accurate Auxiliary Basis Sets for RI-MP2 and RI-CC2 Calculations for the Atoms Rb to Rn. *Theor. Chem. Acc.* **2007**, *117* (4), 587–597. https://doi.org/10.1007/s00214-007-0250-5.

(66) Weigend, F. Hartree–Fock Exchange Fitting Basis Sets for H to Rn. *J. Comput. Chem.* **2008**, *29* (2), 167–175. https://doi.org/10.1002/jcc.20702.

(67) Marenich, A. V.; Cramer, C. J.; Truhlar, D. G. Universal Solvation Model Based on Solute Electron Density and on a Continuum Model of the Solvent Defined by the Bulk Dielectric Constant and Atomic Surface Tensions. *J. Phys. Chem. B* **2009**, *113* (18), 6378–6396. https://doi.org/10.1021/jp810292n.

(68) Neese, F. The ORCA Program System. *WIREs Comput Mol Sci* **2012**, *2* (1), 73–78. https://doi.org/10.1002/wcms.81.

(69) Neese, F. Software Update: The ORCA Program System, Version 4.0. *Wiley Interdiscip. Rev. Comput. Mol. Sci.* **2018**, *8* (1), e1327. https://doi.org/10.1002/wcms.1327.

(70) Neese, F. Software Update: The ORCA Program System—Version 5.0. *WIREs Comput. Mol. Sci.* **2022**, *12* (5), e1606. https://doi.org/10.1002/wcms.1606.

(71) Lehtola, S.; Steigemann, C.; Oliveira, M. J.; Marques, M. A. Recent Developments in Libxc—A Comprehensive Library of Functionals for Density Functional Theory. *SoftwareX* **2018**, *7*, 1–5. https://doi.org/10.1016/j.softx.2017.11.002.

(72) Valeev, E. F. Libint: A Library for the Evaluation of Molecular Integrals of Many-Body Operators over

Gaussian Functions, 2024. http://libint.valeyev.net/.

(73) Luchini, G.; Alegre-Requena, J. V.; Funes-Ardoiz, I.; Paton, R. S. GoodVibes: Automated Thermochemistry for Heterogeneous Computational Chemistry Data. *F1000Research* **2020**, *9* (291), 291. https://doi.org/10.12688/f1000research.22758.1.

(74) Ribeiro, R. F.; Marenich, A. V.; Cramer, C. J.; Truhlar, D. G. Use of Solution-Phase Vibrational Frequencies in Continuum Models for the Free Energy of Solvation. *J. Phys. Chem. B* **2011**, *115* (49), 14556–14562. https://doi.org/10.1021/jp205508z.

(75) Virtanen, P.; Gommers, R.; Oliphant, T. E.; Haberland, M.; Reddy, T.; Cournapeau, D.; Burovski, E.; Peterson, P.; Weckesser, W.; Bright, J.; van der Walt, S. J.; Brett, M.; Wilson, J.; Millman, K. J.; Mayorov, N.; Nelson, A. R. J.; Jones, E.; Kern, R.; Larson, E.; Carey, C. J.; Polat, İ.; Feng, Y.; Moore, E. W.; VanderPlas, J.; Laxalde, D.; Perktold, J.; Cimrman, R.; Henriksen, I.; Quintero, E. A.; Harris, C. R.; Archibald, A. M.; Ribeiro, A. H.; Pedregosa, F.; van Mulbregt, P. SciPy 1.0: Fundamental Algorithms for Scientific Computing in Python. *Nat. Methods* **2020**, *17* (3), 261–272. https://doi.org/10.1038/s41592-019-0686-2.

(76) Hindmarsh, A. C. ODEPACK, a Systemized Collection of ODE Solvers. *Sci. Comput.* **1983**.

(77) Besora, M.; Maseras, F. Microkinetic Modeling in Homogeneous Catalysis. *WIREs Comput. Mol. Sci.* **2018**, *8* (6), e1372. https://doi.org/10.1002/wcms.1372.

(78) Rush, L. E.; Pringle, P. G.; Harvey, J. N. Computational Kinetics of Cobalt-Catalyzed Alkene Hydroformylation. *Angew. Chem. Int. Ed.* **2014**, *53* (33), 8672–8676. https://doi.org/10.1002/anie.201402115.

(79) Geddes, J. A. The Fluidity of Dioxane—Water Mixtures1. *J. Am. Chem. Soc.* **1933**, *55* (12), 4832–4837. https://doi.org/10.1021/ja01339a017.